AN ABSTRACT OF THE THESIS OF

Trevor Howard for the degree of Master of Science in Nuclear Engineering presented on April 24, 2015.

Title: An Approach to Modeling Fuel Plate Deformations in Fluid-Structure Interactions

Abstract approved:_____

Wade R. Marcum

As computational power increases, so does the desire to use fluid-structure interaction (FSI) software to design complex systems and components such as fuel plates. Presently, an effort is underway to support the design and qualification of a new nuclear fuel material which is intended for applications in select, plate-type, research and test reactors. Because of the high flow velocities which are experienced within these reactors, a safety parameter of interest is the onset of plate deformation and potential of plate-to-plate collapse. Using FSI software for the entire design process is tempting; however, utilizing FSI software for large, complex systems requires large quantities of computational resources. Currently, computing FSI solutions using off-the-shelf software of components as small as individual fuel plates can take weeks on a desktop computer, thus requiring the use of multiple servers or a cluster to enable a pragmatic solving time. Since computational resources are valuable, the pertinent question to ask is whether or not the resources being used are a necessity. Fluid structure interaction simulations provide a wealth of information regarding flow patterns, but many practical engineering problems do not require such a detailed solution form. If acceptable solutions could be obtained without solving the entire flow field, the required computational resources may be reduced by orders of magnitude. The study detailed herein presents an alternative approach to solving FSI problems using a one dimensional, semi-analytic model derived from first principles. The resulting approach is much less computationally expensive than

the alternative of leveraging off-the-shelf FSI software. The FSI model developed herein is specific to solving plate deformations (single plates and arrays of plates). A qualitative benchmark of this study's model is made against an analytic solution ABAQUS. Results are then compared against experimental data collected for a single plate acquired by the University of Missouri, as well as experimental data collected for an array of six plates acquired by at Oregon State University. The outcome of this work has resulted in a new modeling approach for FSI problems applied toward flat plate geometry. Results from this new model approach (while limited) compare reasonably well to commercially available software (ABAQUS) and experimental data over a wide range of flow conditions.

An Approach to Modeling Fuel Plate Deformations in Fluid-Structure Interactions

by

Trevor Howard

A THESIS

Submitted to

Oregon State University

in partial fulfillment of
the requirements for the
degree of
Master of Science

Presented April 24, 2015
Commencement June 2015

Master of Science thesis of Trevor Howard presented on April 24, 2015.

APPROVED:

_____

Major Professor, representing Nuclear Engineering

_____

Head of the Department of Nuclear Engineering and Radiation Health Physics

_____

Dean of the Graduate School

I understand that my thesis will become part of the permanent collection of Oregon State University libraries. My signature below authorizes release of my thesis to any reader upon request.

_____

Trevor Howard, Author

ACKNOWLEDGEMENTS

I would like to thank my friends, family, and colleagues. They have provided much support and made graduate school an amazing experience.

I would like to thank my advisor Dr. Marcum for being a wonderful advisor. His support and guidance provided the foundation for my success in graduate school.

Finally, I would like to thank my parents who instilled in me the idea I should strive to achieve more and whose love and support helped me get where I am today.

TABLE OF CONTENTS

TABLE OF CONTENTS (Continued)

LIST OF FIGURES

LIST OF TABLES

An Approach to Modeling Fuel Plate Deformations in Fluid-Structure Interactions

1 INTRODUCTION

With the advent of the Global Threat Reduction Initiative (GTRI) there has been a renewed interest in designing plate-type fuels of new material composition for use in select civilian research and test reactors. The GTRI requires all test and research reactors to convert from Highly Enriched Uranium (HEU) to Low Enriched Uranium (LEU) fuel. For some reactors, such as Training, Research, Isotopes, General Atomic (TRIGA) reactors, conversion can be achieved with the addition of more fuel elements. For plate type reactors, this is not the case. In order to achieve criticality, let alone a reasonable neutron flux, HEU cannot simply be replaced with LEU equivalent fuel. Instead, new LEU fuel must be designed.

One of the consequences of using new materials for fuel fabrication is the need for hydro-mechanical testing and design to support an altered design basis which impacts safety related parameters in such reactors. Nuclear fuel plates are very thin (on the order of 1 mm) with coolant channels being slightly larger. Conducting experiments for the purpose of testing fuel plates designed for use in a reactor is a long and costly process; a large effort is therefore placed in designing the elements before physical testing takes place in order to reduce the amount of testing required. One aspect of fuel element design which has proven to be important in maintaining the fuel's mechanical integrity over the course of its in-pile life is placed on coupled fluid-structure interaction (FSI) simulations [1].

Typically, FSI simulations comprise a computational fluid dynamics (CFD) solver coupled (either explicitly or implicitly) with a computational structural mechanics solver (CSM). Current advances in computational power and discrete numerical methods have provided the ability for great insight into FSI of countless components and systems, including plate type fuels. Unfortunately, the use of software packages for large or

complex geometries is computationally expensive, and in many cases prohibitive based on limited availability of such resources. Time-cost considered, many of the computed results from these software packages are excessive when the goal of the simulation is to determine macro-scale phenomenon such as plate collapse and deflection profiles. The objective of the work presented herein is to further simplify the modeling techniques used to solve the complex FSI problem down to bulk parameters and achieve an acceptable solution expediently. An expedient solution is achieved by leveraging the exact solution for heterogeneous plate deflection under uniform loading within the solid domain and coupling it to an iteratively computed flow distribution solution derived from first principles with appropriately applied correlations within the fluid domain. In this study, a step-wise process is detailed in the development, and qualitative benchmark of an FSI computational model for plate-type geometry. The solution of deflection for a single plate within the solid domain is first compared against the computational results acquired via an off-the-shelf finite element analysis (FEA) code ABAQUS. The plate is then coupled to the fluid domain, having two flow channels adjacent to it and compared against experimental data collected under several boundary conditions. Lastly, the use of the qualitatively validated model is expanded to represent an element which is presently being tested to support the qualification of a new fuel material – the Generic Test plate Assembly (GTPA) (a six plate, seven channel assembly). Results throughout maintain agreement with exceptions, explicitly demonstrating the limitations to the model and method.

1.1 Document Overview

This thesis consists of the following outlined content.

Chapter 1: Introduction – An introduction of the work providing the basis of understanding and motivation of the thesis as well as an overview of the later chapters.

Chapter 2: Survey of Literature – A survey of available literature pertaining to plate deformation under various boundary conditions. The chapter subdivides the current literature into three primary categories: fluid dynamics, structural mechanics, and fluid-structure interactions.

Chapter 3: Theory and Development – The theory behind plate deformation and fluid flow in channels is presented along with the development of the method and formulation of equations utilized to complete this work. The theory and development section describes the model and how it converges upon a solution.

Chapter 4: Model Verification – The model is compared to flow solutions and structural solutions. Verification and expected accuracy of the model as well as various design challenges which were overcome.

Chapter 5: Results and Discussion – The model is compared to two experimental studies, first a single plate model for which deflections were completely characterized. The second is a six plate model which has pressure data and post testing deflection data.

Chapter 6: Conclusion – The conclusion focuses on the implications of the model as well as potential future work associated with the design.

2 SURVEY OF LITERATURE

The literature reviewed herein has been divided into three primary categories based on its importance to the development of the model. The first category delves in to the field of fluid mechanics. Beyond the basics of the fluid mechanics there are three main components important to the development of the model. The effect of high-aspect ratios on fluid flow, the friction loss effects as a result of these channels, and the minor loss effects associated with the plate entrant and exit boundary conditions are such components. For the second section, structural mechanics, it is important to distinguish between a wide-beam and real-plate deflections, and the effects of heterogeneous compositions. The final category is the literature involved with fluid-structure interactions. For the geometry and model, the three types of FSI categories that are important are fluid induced plate deflection, plate flutter, and theoretical and numerical FSI. While other FSI components such as vortex shedding may play a role in the overall deflection, these aspects are not detailed within the framework of the model.

Each of the following sections is detailed as:

1. Fluid Mechanics
    a. High-Aspect Ratio Channels
    b. Minor Loss Effects
    c. Frictional Loss Effects
2. Structural Mechanics
    a. Wide-Beam Deflection
    b. Real Plate Deflection
    c. Heterogeneous Compositions
3. Fluid-Structure Interactions
    a. Plate Deflection and Collapse
    b. Plate Flutter
    c. Theoretical and Numerical FSI

In Table 2.1 the three categories and sub-categories have been listed as individual items as well as the reference number. Of the sections listed above, an “X” has been placed under the categories for which the reference applies. Each section is discussed in further detail later.

Table 2.1: Reference material

	Categories as Listed Above								
Reference Number	1.a.	1.b.	1.c.	2a.	2b.	2c.	3a.	3b.	3c.
[1]							X	X	
[2]	X		X						
[3]		X					X		
[4]		X	X						
[5]		X	X						
[6]	X	X	X						
[7]	X	X	X						
[8]	X	X	X						
[9]				X		X	X		
[10]				X		X			
[11]							X	X	
[12]								X	
[13]								X	X
[14]							X		X
[15]							X	X	X
[16]							X	X	
[17]							X		X
[18]							X	X	
[19]							X	X	
[20]								X	X
[21]								X	
[22]							X		
[23]							X	X	
[24]								X	X

2.1 Fluid Mechanics

Most fluid textbooks provide a general background for the fluid mechanics driving the pressure differential which creates the load on the plate. These sources provided the basis for the fluid mechanics equations used to write the code. White, Nunn, and Panton provided basic formulas for the use of minor loss coefficients and friction factors [4-6]. As seen in the textbooks previously mentioned, the majority of research which has been conducted on fluid mechanics for internal flow has traditionally centered on generic geometric forms such as pipes or ducts. The bulk characterization of pressure loss

through a piping system (or narrow flow channel) may be divided into minor losses and major losses. The calculation of the major and minor loss terms is dependent upon geometry. The geometries presented in textbooks tend to have aspect ratios near unity. However, the nuclear fuel considered herein uses high-aspect ratio flow channels which present a unique challenge. High-aspect ratio channels have limited applications and as such these channels are often not discussed in the context of standard fluid mechanics text books. While all cited sources provided great insight, none detailed cases where the geometry varied significantly from generic pipe flow. An article by Jones, however, provided an enhancement to the turbulent friction factor for high-aspect ratio rectangular ducts [2]. While Jones' article presented on the friction factor, there was no correlation for form losses of finite plate arrays. To determine the form loss term, two references stand out in particular. The first reference is the Applied Fluid Dynamics Handbook which provides a wealth of information regarding atypical geometries, friction factors, and form losses, including large arrays of plates [7]. The latter was a numerical study performed by Roth which utilized the six plate geometry mentioned herein [8]. The study provided detailed pressure drop results along the flow path which may be used to determine the form loss coefficient associated with the geometry.

2.2 Structural Mechanics

Important considerations must be made for the appropriate handling of the structural mechanics under a load. With respect to plate-deformation, many models assume wide-beam theory to simplify the calculations, resulting in a fourth order polynomial deflection profile along a plate's span-width and no out-of-plane deflection. This, however, does not reflect the exact solution for deflection of a plate which may have appreciable components of deflection in the out-of-plane direction. While the numerical handling of the deflection profile between wide-beams and plates are important, the inclusion of appropriate information relating to the composition of the plate is equally important. Two models provided insight toward the nature of heterogeneous plate deformation and implementation of multiple material properties. An article by Jensen investigated the

change in Miller's critical velocity by changing a homogeneous plate into a heterogeneous composite [9]. An extension of the aforementioned work was completed by Marcum and investigated the effects of adding a heterogeneous region to the plate near the supports [10].

2.3 Fluid-Structure Interaction

Articles based on fluid structure interactions provided the best information on the physics involved in the analysis of the parallel plate flow. With respect to this study's focus (plate-type fuel geometry), the most extreme scenario which may result from FSI is that of plate collapse (plate-to-plate contact). During plate collapse, two plates separated by a single flow channel are drawn together by a pneumatic load. The collapse results in a reduction of heat removal capability and an immediate rise in local surface temperature may lead to eventual fuel failure. Several studies provided calculations and predictions pertaining to plate collapse [3, 9, 12, 14-19, 22]. The genesis of these works can be traced back to the theoretical work done by Miller in 1958 [14]. More importantly, Miller provided the eponymous critical velocity further detailed in section 3.1. Miller's critical velocity is derived from inviscid flow and stability theory. As a result it is a powerful analytical relation for predicting when the deflection in a plate becomes significant. Kane further expanded on Miller's critical velocity by quantifying how deviations in the form losses at the inlet would affect deflections in the plate and eventual plate collapse [3]. While plate collapse is of interest, plate flutter is also an important phenomenon as it can occur as a result of pressure waves in the fluid or as a result of vortex shedding at the frequency which aligns with a plate's natural frequency. While vortex shedding is not modeled, pressure waves may occur in the solution developed herein resulting in flutter. Flutter won't be present in this study's final solution; however, causes of flutter are important to understand as they may lead to numerical instabilities in the code. From the experimental side, Groninger, Smissaert and Zabriskie observed flutter around twice that of Miller's critical velocity [15, 16, 18, 19, 22]. The flutter observed is reminiscent of the observed flow induced flutter observed in free blunt bodies [21, 24]. Flutter and the

stability of both single and parallel plate assemblies has been studied in depth [1, 9, 11-16, 18-20, 22, 23]. Most studies determine a critical velocity at which the deformations become very large, or the plate becomes unstable. The synthesis of the work, both experimental and theoretical in nature, provides great insight into the deformations and instabilities associated with fluid flowing past plates.

3 THEORY AND DEVELOPMENT

3.1 Plate Collapse

In 1958, Ronald Miller predicted plate collapse by combining wide-beam and inviscid flow theory. Miller's relationship determined the point at which the dynamic pressure forces would supersede those of the plate's restorative forces [14]. The relationship which Miller derived was designed for an array of plates with symmetric channels. Although the relation was derived for symmetric channels in an array, further modifications can be made to account for a single plate with asymmetric spacing. In the case of an array, plates deflect towards or away from each other. The result is a change in channel area twice the integral deflection of one plate. With only one plate, the change in gap size is exactly the integral deflection of the plate; thus, Miller's critical velocity for a single plate is a factor of $\sqrt{2}$ greater than Miller's critical velocity for an array of plates [19]. In section 4 the gap thicknesses are not constant as is the case with Miller and Zabriskie's studies [1, 8, 14, 19]. With further analysis, one can derive the change in Miller's velocity due to asymmetry. The change per unit cross-sectional area, given as

$$\frac{\Delta A}{A_o} = \frac{\left(1-\upsilon^2\right) p b^4}{60 E a^3 h}, \tag{1}$$

can be determined by: $A_{o,}$ the flow channel original cross sectional area; ΔA, the change in cross sectional area of the flow channel; υ, Poisson's ratio of the plate; b, the plate span-width; p, the mechanical load on the plate; a, the plate thickness, E, Young's modulus of the plate; and h, the channel height. Noting h is not specific for a respective flow channel which separates the plate, the relation in (1) is limited to a geometry which assumes symmetric channels. Because this study is interested in identifying the influence of the hydro-dynamic response of the flow field on a single plate with asymmetric channels, it is more appropriate to use the average channel height and flow area,

$$A_o = \frac{A_{1,o} + A_{2,o}}{2}, \tag{2}$$

where subscript 1 and 2, represent characteristics of flow channel 1 and channel 2, respectively. If the flow channel widths of each channel are equal, then the average channel height may be reduced to

$$h_o = \frac{h_1 + h_2}{2}. \tag{3}$$

From Bernoulli's equation, the pressure load on the plate per area change is equivalent to the change of the velocity squared,

$$\frac{p}{\Delta A} = \frac{\rho}{2\Delta A}\left(\left(\frac{v_o}{1-\frac{\Delta A}{A_1}}\right)^2 - \left(\frac{v_o}{1+\frac{\Delta A}{A_2}}\right)^2\right). \tag{4}$$

In (4) p is pressure resulting from a change in cross sectional area via a Bernoulli effect, v_o is the initial flow channel superficial fluid velocity, and ρ is fluid density. As ΔA approaches null, the limit of the right hand side of (4) can be solved for pressure (p), resulting in

$$p = \frac{\left(1+A_r\right)^2}{A_r}\frac{\rho v_o^2}{2}\frac{\Delta A}{A_o}. \tag{5}$$

As would be expected, replacing A_r with its reciprocal in (5) yields the same solution. One can utilize the method developed by Miller to arrive at a generic form of the critical flow velocity for a single plate with both edges clamped which is asymmetric between two adjacent flow channels,

$$v_c = \frac{2}{1+A_r}\left(\frac{30A_rEa^3h_o}{\rho b^4\left(1-\upsilon^2\right)}\right)^{1/2}. \tag{6}$$

To confirm the relation presented in (6), its form should return to the fundamental form derived by Ronald Miller [14] as A_r approaches unity. Through inspection, taking A_r to unity produces

$$v_c = \left(\frac{30Ea^3h_o}{\rho b^4\left(1-\upsilon^2\right)}\right)^{1/2}, \tag{7}$$

analogous to the relation developed by Miller [14], and exactly Zabriskie's relation [19]. At the opposite end of the spectrum, forcing A_r to infinity yields

$$v_c = \left(\frac{60Ea^3 h_{min}}{\rho b^4 \left(1-\upsilon^2\right)} \right)^{1/2}, \tag{8}$$

where h_{min} is the channel height of the smaller channel. Thus, there is a limit to the maximum Miller's critical velocity for asymmetric channels. Miller's velocity can be further modified using relationships posed by Kim [12]. The relation accounts for both single plates and arrays and shows the expected critical velocity is slightly higher than Miller's critical velocity.

In the case of fuel plates, the critical velocity is altered relative to a homogeneous plate due to the presence of the fuel within a cladding. Equation (6) can be better utilized by substituting in

$$D = \frac{Ea^3}{12\left(1-\upsilon^2\right)}, \tag{9}$$

flexural rigidity $(D \equiv EI)$. In doing so, one can calculate the flexural rigidity for a laminate plate and, respectively, the critical flow velocity as outlined by Jensen [9]. More in-depth relations and solutions are presented by Guo determining the instability of a plate [11] or array of plates [23]. However, Guo's work assumes a free-free boundary condition on the sides of the plates, not the clamped-clamped boundary condition present in most nuclear reactor fuel plates.

Currently, the most conservative basic-model approach for the purpose of predicting fuel plate deflection is the 'dynamic pressure model' [17]. It assumes the pressure disparity between two channels is at its most extreme. The dynamic pressure model applies the dynamic pressure to determine the deflection of the plate as a uniform wide beam. The plate loading of the dynamic pressure model is specifically the dynamic pressure,

$$p = \frac{1}{2}\rho v^2. \tag{10}$$

The dynamic pressure model assumes plate deflection is based on the loss of flow, or stagnation of a fluid in a discrete channel adjacent to said plate. It is shown to be accurate in a certain range for specific problems. At higher flow rates, the model tends to vastly over-predict the deflection seen in the plate [17].

Alternatively, one could turn to a more computationally expensive and accurate method for calculating deflections in the channel through use of a coupled CFD-CSM solver or computational FSI program. Computational FSI is commonly utilized within organizations possessing vast computational resources and sufficient time to allow a solution to result which is valid and independent of spatial and temporal model refinement. Unfortunately, computational FSI techniques are often not practical and available for many researchers, engineers, and scientists interested in acquiring a relatively robust, comprehensive, and accurate solution. An alternate approach to the traditionally considered CFD-CSM solvers is to leverage analytical models for fluid flow and plate deformation for use in a fully integrated FSI domain. This study achieves the aforementioned approach by comprehensively characterizing the fluid-structure interaction of an array of flat plates with variable boundary conditions and channel geometries.

An important characteristic of plates in axial flow is the onset of flutter, or the general dynamic instability associated with the plate above a critical velocity. Flutter is a phenomenon observed in plates as well as any non-circular body. Flutter occurs when the reduced velocity,

$$v^* = \frac{v}{f_n a}, \tag{11}$$

is satisfied. From (11) v is the fluid velocity and f_n is the plate frequency (of relevance when it exceeds 20); however, flutter has been witnessed in reduced velocities as low as unity [24]. Plate flutter has recently been study by Eloy [21] which examined plate dynamics under a single fixed boundary condition. A solution for parallel plates under a single fixed boundary has been proposed by Michelin [13]. Additionally, flutter and

deformations involved with nuclear fuel plates has been examined since Miller derived the critical velocity [14,15,17-19,21]. While the studies focus on nuclear fuel plates – which are composite in nature – the experiments are often conducted using a homogeneous plate and the analytic solutions assume a homogeneous composition.

3.2 Description of Model

One objective of the model is to obtain a reasonable solution. In order to determine whether or not the solution is reasonable, the solution developed by this study must be compared to experimental data. The bulk of the available data for plate deflection and flow fields comes from the hydro-mechanical fuel test facility (HMFTF), located at Oregon State University (OSU). Several tests were conducted between 2012 and 2014 using a specialized element called the generic test plate assembly (GTPA).

The GTPA frame is designed for versatility, allowing the channel gaps (flow channels adjacent to each plate) to be varied so a range of channel gaps may be evaluated if necessary. The GTPA design is modular, so the test plates may be assembled into the complete GTPA prior to each test and disassembled at the conclusion of each test. By designing the GTPA in such a modular manner, its frame may be used for all of the test plate sets, reducing the number of mechanical components requiring fabrication. Support combs are inserted between the plates at the inlet and the outlet of the channels. These combs limit the plate deflection at the inlet and outlet so that maximum deflection takes place in the interior of the experiment assembly (where the fueled region is located on a plate) instead of at the inlet and outlet; this allows for a quantitative comparison of the various fuel meat types and their relative resistance to hydraulic forces to be made. These combs are inserted into each channel at the center of the plate width. The GTPA is designed such that comb use is optional.

The GTPA can be seen in Figure 3.1. Figure 3.1 (a) presents the modular GTPA in a disassembled configuration; Figure 3.1 (b) shows the GTPA after assembly and placed

onto the experimental hardware, prior to being placed within the test section of the HMFTF at OSU. One of the central two plates is referred to as the Test plate while all other exterior plates are known as the Hydraulic plates. A single Test plate was chosen in order to provide asymmetry to the GTPA. This asymmetry is intended to provide more repeatable experimental results from trial-to-trial as compared to a symmetric GTPA. During all tests performed under this work-scope the Hydraulic plates are comprised of Inconel [25]. The Test plate will be one of the following material configurations: aluminum 6061-O Temper, aluminum clad DU-Mo monolithic foil, or aluminum clad, aluminum-stainless steel dispersion, depending on the test. This design provides for the appropriate hydraulic boundary conditions to be set via the hydraulic plates while mechanical displacement is achieved via the Test plate.

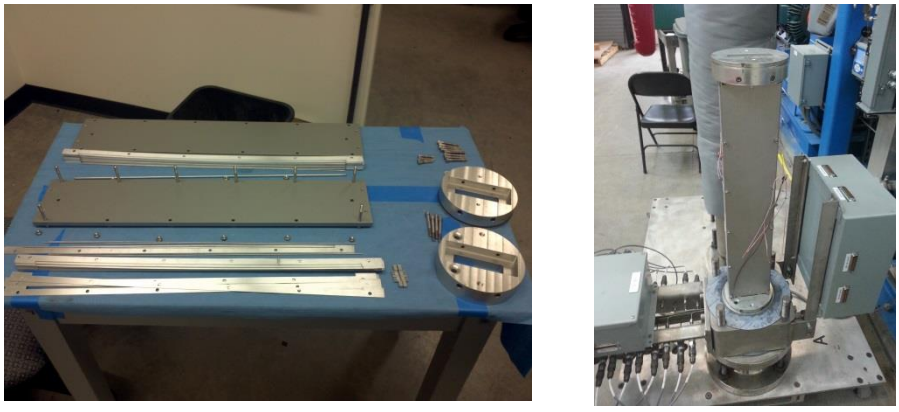

(a) (b)

Figure 3.1: GTPA disassembled (a) and assembled (b)

All flow channel thicknesses are equally spaced to a nominal 0.075 inch height with the exception of the central channel which is adjustable in thickness to facilitate flow biasing and therefore inducing hydraulic loading on the central plates. There are six variably designed thicknesses for the central flow channel which are outlined below in Table 3.1. The wire separators simulate pinned edge boundaries for the Test plate, all other plates will emulate clamped edged boundaries. All test plates are similar in nominal geometry (24 inches long, 4 inches wide, and 0.05 inches in thickness).

Table 3.1: GTPA Geometric Configuration Summary

GTPA Geometric Case [#]	Nominal Channel Thickness [inches]	Central Channel Thickness [inches]
1	0.075	0.102
2	0.075	0.106
3	0.075	0.118
4	0.075	0.125
5	0.075	0.188
6	0.075	0.225

The plates were made entirely of aluminum for the initial testing and were aluminum for the experimental results in section 4.4 . After the first few verification tests it was decided to replace five of the outer plates with Inconel shown as green in Figure 3.2 and dark grey in Figure 3.3. These plates provided a more rigid boundary condition around the plate being tested. By substituting Inconel for aluminum, the deflections observed in the test plate were more consistent.

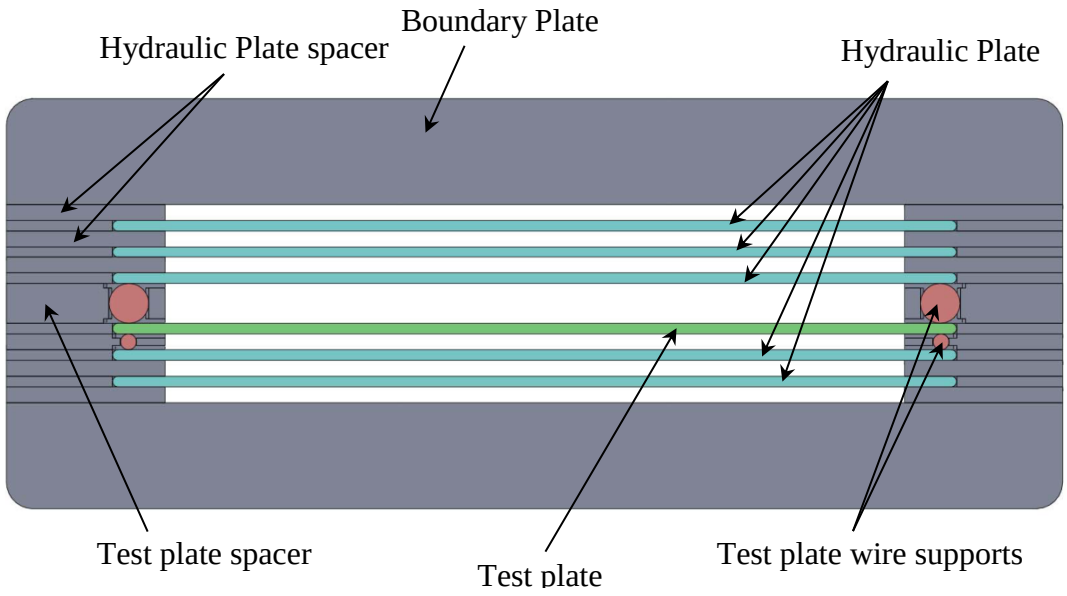

Figure 3.2: Top-down view of the GTPA

Figure 3.2 shows the GTPA as assembled. There are a total of five hydraulic plates which are comprised of either Inconel or aluminum. The test plate can either be fueled or aluminum and uses and spacer and wire supports to achieve the desired boundary conditions. The five hydraulic plates maintain a clamped boundary condition whereas the test plate wire supports allow for the test plate to have pinned boundary conditions.

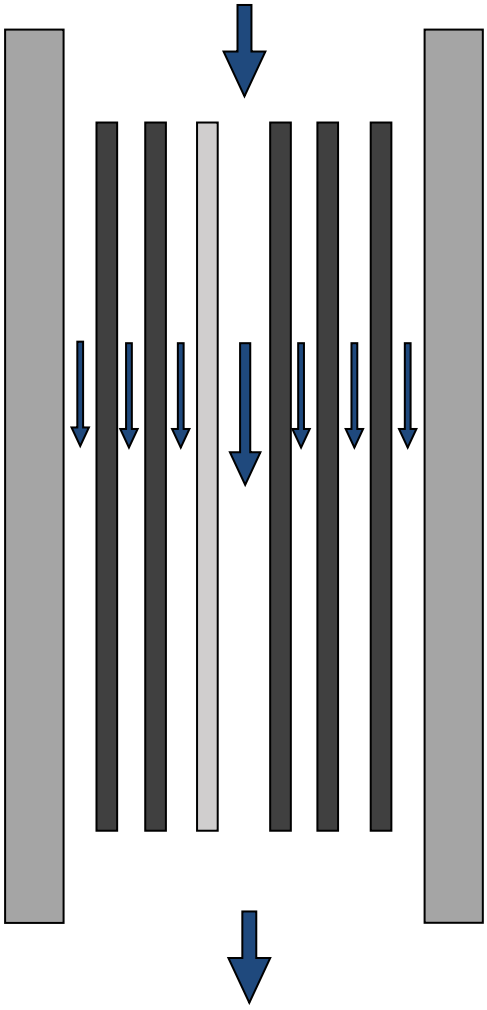

Figure 3.3: GTPA model geometry

Figure 3.3 shows the side view of the GTPA. The test plate is seen in light gray and the hydraulic plates are dark grey. The thicker boundary plates are shown as well on the outside. During the testing the central channel maintains the largest amount of flow up until plate collapse occurs.

While the end goal is to develop the model for a six plate system, effort is given herein to develop a nomenclature that works for any number of plates. The easiest way of achieving the desired outcome is setting the numerical model to solve a single plate in a channel. Single-plate geometry allows for an expedient understanding of the model process and design. Additionally, the single plate model is less complex to verify and thus a pre-requisite for the six plate, or any multi-plate model. In a single plate model, only one plate is deflecting and the gap size is only a function of the deflections of the single plate. A study conducted by Kennedy provided experimental data to qualitatively validate the model for a single plate [1]. A representation of the model domain is shown in Figure 3.4.

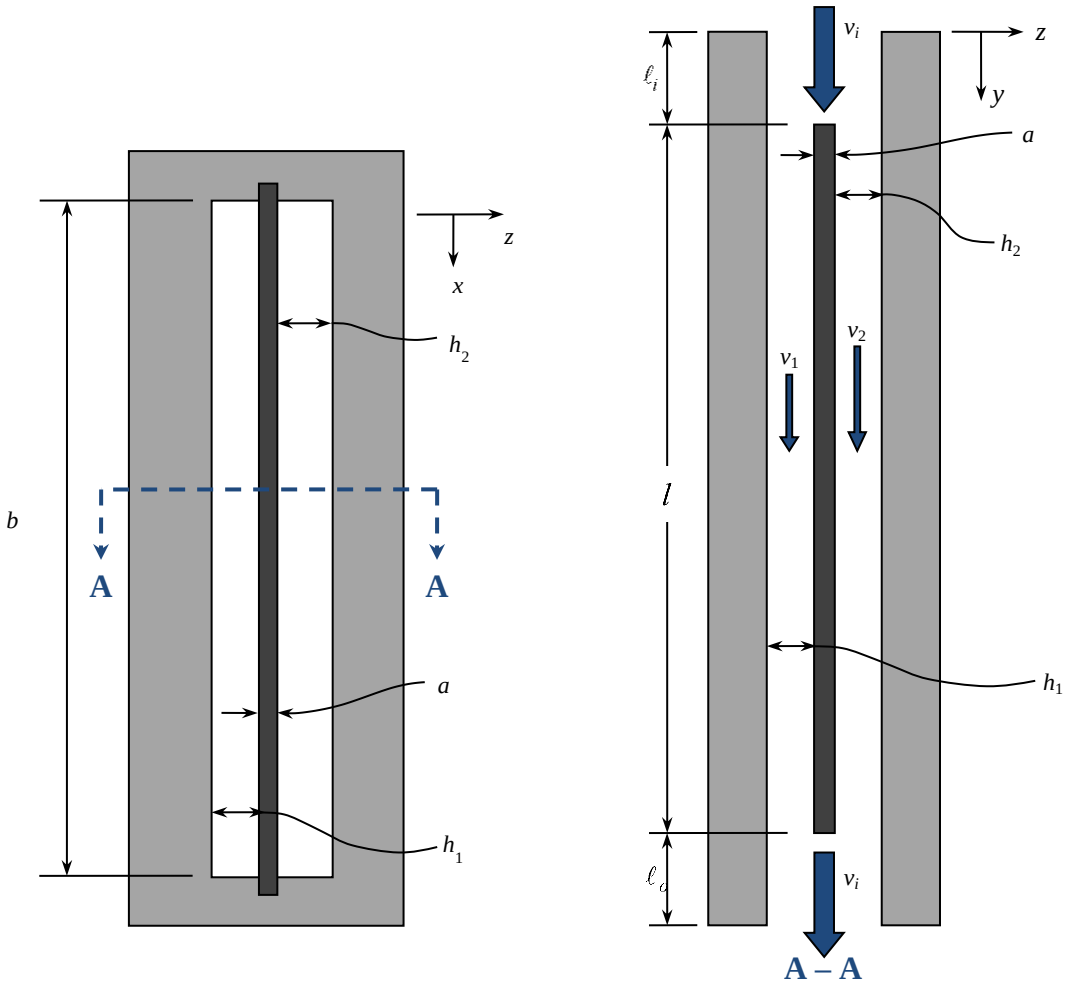

Figure 3.4: Model geometry (a) cross section and (b) axial-length cut view

In Figure 3.4, the plate is secured to the wall of the channel along the *y*-*z* faces via a clamped-clamped (CC) boundary condition; the remaining faces remain free. Water flows through the channel in the *y*-direction. The gap between the *x*-*y* faces of the plate and the channel are different between the top and bottom, thus resulting in the flow disparity and plate deflection.

3.3 Wide-Beam Theory

It is necessary to begin the method development with the most fundamental form of a uniformly distributed load (w) on a beam; given as

$$D\frac{d^4z}{dx^4} = w, \tag{11}$$

where D is the flexural rigidity of the beam, z is the deflection and x is the span-wise direction. The above equation has a well-known exact solution for beams where both edges simply supported (SS), one edge simply supported and the other clamped (CS), or both edged clamped (CC) [10]. For this study, the exact solution for the deflection of a wide-beam is utilized to solve the solid-domain response to a hydraulic load.

3.4 Fluid Dynamics

For the fluid fields, the pressure loss associated with the flow can be determined from the Navier-Stokes equations. The case described herein looks at the Navier-Stokes equation in the y-direction for an incompressible fluid with constant properties,

$$\rho\left(\frac{\partial v}{\partial t} + \left(\bar{u}\cdot\nabla\right)v\right) = -\frac{dp}{dy} + \mu\nabla^2 v\,. \tag{12}$$

Furthermore, (12) is reduced to a one velocity component for a steady state system,

$$\rho\left(v\frac{dv}{dy}\right) = -\frac{dp}{dy} + \mu\nabla^2 v\,. \tag{13}$$

Linearization of (13) yields the Darcy-Weisbach Equation,

$$\Delta p = \frac{\rho v^2}{2}\left(f\frac{l}{d} + k\right), \tag{14}$$

where f is the friction factor, l is the length along the flow direction, d is the hydraulic diameter, and k is the form loss coefficient. The flow area is formed by a rectangular shape; therefore the hydraulic diameter is most appropriately characterized as,

$$d = \frac{4A}{\eta}, \tag{15}$$

where η is the wetted perimeter. It is assumed the friction factor can be described as

$$f = \frac{64}{\mathrm{Re}} \tag{16}$$

under laminar flow conditions and

$$\frac{1}{f^{\frac{1}{2}}} = -2.0 \log\left(\frac{\frac{\epsilon}{d}}{3.7} + \frac{2.51}{f^{\frac{1}{2}} \mathrm{Re}} \right) \tag{17}$$

when the flow is turbulent in each respective flow channel [5]. Since the friction factor is dependent upon itself, an iterative process must be used. Currently the minor loss term at the entrance is described by the equation for a sudden contraction (k_{sc}),

$$k_{sc} = 0.42\left(1 - \frac{d_n^2}{d_3^2}\right), \tag{18}$$

where d_n is the hydraulic diameter of either channel 1 or 2, and d_3 is the hydraulic diameter of the inlet region. Equation (18) is valid for a diameter squared ratio of 0.76 after which, the sudden expansion equation can be used [5]. At the outlet, the fluid undergoes a sudden expansion which is described as

$$k_e = \left(1 - \frac{d_n^2}{d_3^2}\right)^2. \tag{19}$$

From here, the original equation for the flow field can be solved using continuity [5]. Non-recoverable losses experienced via channel 1 must be the same as the non-recoverable losses experienced via channel 2. In other words,

$$\Delta p_1 = \Delta p_2 . \tag{20}$$

Second, the mass flow rates must be conserved, thus,

$$\dot{m}_1 + \dot{m}_2 = \dot{m}_3 . \tag{21}$$

Mass flow rate is defined as

$$\dot{m} \equiv \rho A v . \tag{22}$$

3.5 Solving the Structural Domain

In the *x*-direction (refer to Figure 3.4), the deflection profile at any given *y* location is assumed to match the profile of a homogeneous wide beam. For a heterogeneous deflection profile solution in the *x*-direction, a model presented by Marcum et al. was leveraged [10]. The model allowed for the utilization of both homogeneous and heterogeneous plates for use in the code.

With the initial model, there are no forces propagated in the *y*-direction. With no communication from one plate section to the next, the deflection profile mimics the pressure profile. With lack of communication between the cells in the *y*-direction, the simulation loses accuracy under steep pressure gradients and collapses at velocities more than 50 percent lower than predicted by experiment. To achieve a more accurate solution, two models were proposed so the plate would represent appropriate resistive loading along the *y*-direction. The first of which was a spring model. The spring model assumes the force between two different elements can be described by the spring equation,

$$F = \lambda \Delta z , \tag{23}$$

where F is a force applied across a distance Δz, to an object having a spring-constant λ. The resulting force is then converted into a pressure load,

$$p = \frac{\lambda \Delta z}{\Delta y b} , \tag{24}$$

where b is the plate width and Δy is the cell size in the *y*-direction. The constant was predicted using the definitions of Young's modulus and the shear modulus, and determined from inspection. The constant was found to be inversely proportional to Δy which played an important role in the implementation of boundary conditions.

The second method was solving the structural equation while forcing a wide beam profile in the *x*-direction and solving for the additional forces using the gradients in the *y*-direction. The "additional term model" allows for the beam to propagate forces in the *y*-

direction while reducing the numerical solution to a one dimensional problem. The equation for plate deflection is defined as,

$$\nabla^2(\nabla^2 Dz) = w, \tag{25}$$

which bears a resemblance to the wide-beam model from equation (11). Expanding out the terms, equation (25) can be written as

$$D\frac{\partial^4 z}{\partial x^4} + D\frac{\partial^4 z}{\partial y^4} + D\frac{\partial^4 z}{\partial x^2 \partial y^2} = w. \tag{26}$$

w is the load on the plate, which is the fluid induced pressure load *P*. If one assumes a wide-beam profile in the *x*-direction, the fourth order term in the *x*-direction can be replaced with a hypothetical load (*w'*). Solving for the new load,

$$w' = P - D\frac{\partial^4 z}{\partial y^4} - D\frac{\partial^4 z}{\partial x^2 \partial y^2}. \tag{27}$$

w' is then applied to the plate at the given *y*-location as opposed to *P* (which would produce the base model solution). The corresponding derivatives in equation (27) can be solved for numerically. The solution was achieved by using a first order central differencing scheme.

3.6 Solving the Fluid Domain

Since the channel is rectangular with a high-aspect ratio, utilizing equation (17) is not entirely appropriate. To account for high-aspect ratio channels, a method is proposed in a study conducted by Jones. The new Reynolds number is determined as,

$$Re^* \equiv \phi^* \,\mathrm{Re}; \tag{27}$$

and the corresponding ϕ^* is a function approximated as,

$$\phi^* \cong \frac{2}{3} + \frac{11}{24}\frac{h}{b}\left(2 - \frac{h}{b}\right). \tag{28}$$

The approximation most resembles the complete equation at high aspect ratios, particularly above 5:1 [2]. While equation (28) modified the value for the friction factor, the modification played only a small role in the overall deflection.

3.6.1 Geometric Losses

Most form loss coefficients are designed for use in nearly circular ducts; however, the problem presented is not circular, but rectangular channels with high aspect ratios. As a direct consequence, some of the terms require modification. Both minor loss terms are functions of the hydraulic diameter squared. The basis of the proportionality is entirely based on convention; however, an alternative approach looked at replacing the diameter squared with the area of the channel. The premise for doing so is the area for a high-aspect ratio channel is proportional to the diameter, not the diameter squared as is the case for circular channels. The diameter ratio is then replaced as

$$\frac{d_n^{\,2}}{d_3^{\,2}} \rightarrow \frac{A_n}{A_3},$$

in equations (18) and (19). The entrance and exit coefficients assume the volume of fluid from the entire channel is being contracted to, or expanded from the volume of the plate channel. For the given geometry, the flow is split, neither fully contracted nor expanded. The fluid area ratio should be determined by the perceived area of the entrant fluid, not the ratio of the channels. The new ratio is determined by the amount of mass flow rate into the channel. The expected area prior to expansion,

$$A_3' = \frac{v_n h_n}{v_3} b, \tag{29}$$

is derived from equations (21) and (22). The original value for the diameter ratio is transformed,

$$\frac{d_n^{\,2}}{d_3^{\,2}} \rightarrow \frac{A_n}{A_3} \rightarrow \frac{A_n}{A_3'},$$

and replaced in equations (18) and (19). The consequences of changing the minor loss coefficient are discussed in section 4.1 .

3.6.2 Acceleration Effects

Using Bernoulli's principle, the change in pressure due to acceleration was also considered after the minor loss at the inlet. The pressure change in the channel,

$$\Delta p_{1,2} = \rho \frac{v_{i,1}{}^2 - v_{i,2}{}^2}{2}, \tag{30}$$

shows the velocity (which is linearly proportional to the area) plays a role in plate deflection. Biased deflection will tend to become more biased as the inlet velocity increases.

3.7 Domain Coupling

Wide-beam theory is, as the name implies, designed for wide-beams. A plate in and of itself is not a wide-beam. However, if the plate were under a uniform load, the wide-beam theory solution would hold for most of the plate. Instead of being represented as a single wide-beam, the plate can be represented as a string of "wide-beams". Under a uniform load the solution wouldn't change, however, if the load changes along the plate, then each "wide-beam" would respond to the load at the given location. The result would be a plate deflection profile respondent to a changing load, or more importantly, the flow conditions. Each wide-beam equation is required to be solved for the deflection, so the plate must be discretized into individual cells. Since the width is clamped, the plate is discretized along the *y*-direction.

The discretization of the plate is not only for use of the wide beam model for a changing load, but for the friction factor as well. The friction factor, instead of being one value, can be determined as a sum of the friction factors of each given cell; thus,

$$f_n \frac{l_n}{d_n} = \sum_{i=1}^{N} f_{i,n} \frac{l_{i,n}}{d_{i,n}}. \tag{31}$$

A problem arises because the average velocity is not the same for every cell. To account for the change in velocity, the nominal velocity for the gap is used in equation (14). The nominal velocity is defined as the channel mass flow rate divided by the density and nominal area (height of the channel (h) multiplied by the width (b)),

$$v_n = \frac{\dot{m}_n}{\rho A_n} = \frac{\dot{m}_n}{\rho b h_n}. \tag{32}$$

Since all calculations are performed with respect to the nominal velocity, the friction factor requires an additional modification to be used in the pressure drop equation based on the ratio of the section average velocity to the nominal average velocity.

$$r_{i,n} = \frac{v'_{\mathrm{i,n}}}{v_n} = \frac{h_n}{h'_{i,n}} \tag{33}$$

where h' is the new height of the channel. Consequently, the pressure drop equation is modified and becomes

$$\Delta p_n = \frac{\rho v_n^2}{2}\left(k_{c_n} r_{1/2,n}^2 + k_{e_n} r_{N+1/2,n}^2 + \sum_{i=1}^{N} f_{i,n} \frac{l_{i,n}}{d_{i,n}} r_{i,n}^2 \right). \tag{34}$$

The coupled interaction is the communication between the structural domain and the fluid domain. Communication is achieved through an iterative process.

3.8 Generic Process

From beginning to completion, the flow solver first determines the cell geometry. If it is the first iteration, the geometry has been defined by the user. The next step is presented by solving the equilibrium equations (20), (21), and (34). Once the equations have been solved, and the fluid velocities determined, the load created by the fluid can be calculated. Additionally, the plate will resist deformations and the “self-load” must be calculated afterwards. The combination of these loads determines the deflection of the plate. With the plate deflected, the cell geometry can be recalculated and the process restarted. A qualitative process can be seen in Figure 3.5.

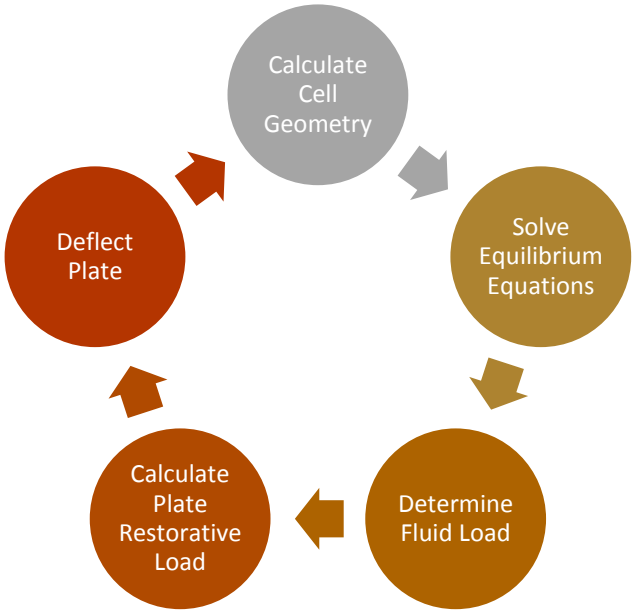

Figure 3.5: Circular flow diagram of the solver

Figure 3.6 shows the entire flow diagram for all process steps of the solver. The loops are color coded to the most inner loop. Prior to running, the initial parameters are used to determine plate deflection and model geometry. Upon start-up of the code, the channel geometry is imported in the form of a .csv file to set a baseline for the initial plate geometry and determine deflection. Once the model is defined, the initial mass flow rate increment is used. The mass flow rate increment is used in the plate deflection model.

With the mass flow rate defined, the first step of the solver is calculating the plate deflections due to the load. For the initial step the load is 0, thus the plates do not deflect. The deflections of the plate are then used to calculate the gap geometry ("calculate cell geometry" in Figure 3.5) and the plate restorative load. The gap geometry is then fed into the flow distribution loop.

Once in the flow distribution loop the mass and momentum equilibrium equations are solved to determine the distribution of flow ("solve equilibrium equations" in Figure 3.5). The values for the modified Reynolds number are calculated in each channel. From there,

the respective friction factor can be calculated. Next, the minor loss terms for the channel are calculated. The initial pressure drop for the first channel is then acquired. Once the pressure drop in the channel is tabulated, the same pressure drop is used for all other channels. Since the given pressure drop is the same for all channels, the velocity of each channel be calculated. If the solution were correct on the first iteration, the mass flow rates of the sum of all of the channels would be equal to the inlet mass flow rate. The reality is the mass flow rates will differ. If the absolute difference between the calculated and defined mass flow rates is too large, or rather, out of tolerance, the nominal velocities are scaled such that the mass flow rates are equal. Upon rescaling the velocities, the loop begins again.

Once the mass flow rate is within tolerance, the loop ends and the fluid load is then calculated ("calculate fluid load" in Figure 3.5). The fluid load is then combined with the plate restorative forces ("calculate plate restorative forces" in Figure 3.5). The combination of forces is then combined into a uniform load. If the change in the load is insignificant when compared to the previous generation, the loop outputs the data as a .mat file and proceeds to the next incremental mass flow rate. If the load is not within tolerance, the plate is then deflected again ("deflect plate" in Figure 3.5) and the process starts over.

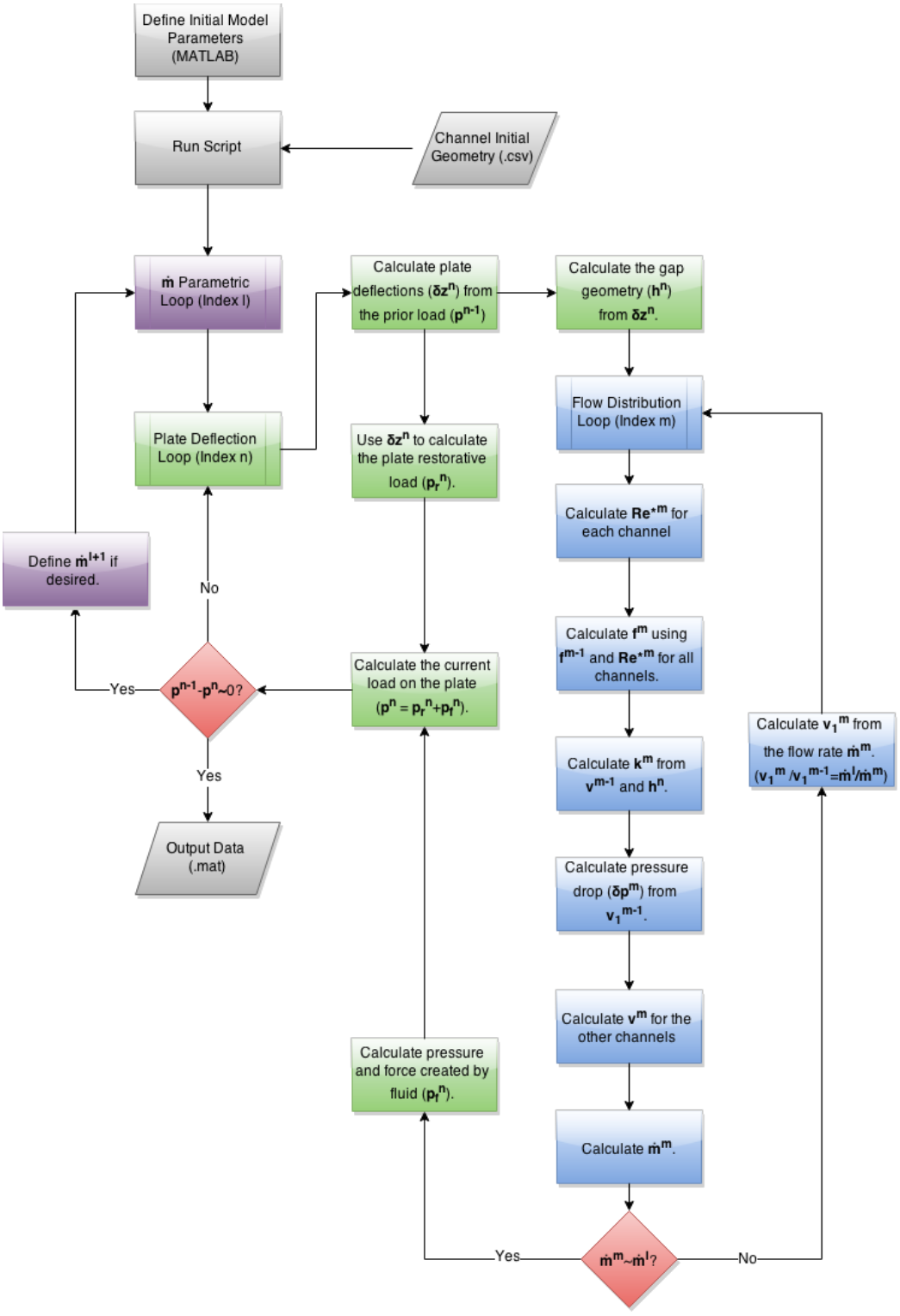

Figure 3.6: Complete flow diagram of the solver

4 MODEL VERIFICATION

4.1 Assessment of Fluid Solver

An initial assessment of the solver verified flow rate conservation over each respective cell; additionally it confirmed the total pressure drop observed across each flow channel summed to an equivalent value. The plate deflection corresponded appropriately to the pressure differential applied. For the purpose of verification, a plate with specific aspect ratios was chosen. The plate was chosen to have a ratio of 1:100:500 (similar in dimensional proportion to results to be further examined herein). Following the initial assessment, a test-case was conducted. The desired outcome of the test case demonstrates alignment with the model's ability to predict the equivalent flow velocity Miller's model predicts under respective conditions. Miller's model assumes there is neither friction nor minor losses involved, additionally the change in mass flow rate within each channel is null. Consequently, the plate deflects as a single solid body, ultimately reaching a point where the forces imposed by the fluid overcome the forces of the plate. The model geometry considered for the test case is presented in Table 4.1.

Table 4.1: Verification plate data

Parameter [Symbol] (unit)	Quantity
Plate length [l] (m)	0.5
Plate width [b] (m)	0.1
Plate thickness [a] (m)	0.001
Young's modulus [E] (GPa)	70
Poisson's ratio [υ] (#)	0.33
Flow channel 1 Height [h_1] (m)	0.002
Flow channel 2 Height [h_2] (m)	0.003
Fluid density [ρ] (kg/m^3)	997
Viscosity [μ] (Pa-s)	0.00088871
Surface roughness [ε] (m)	0.0000015
Spring constant [λ] (MN/m)	300

Explicitly computing the solution from equation (6) yields a fluid velocity of 7.532 m/s. Since the goal is to compare the analytic solution to the developed code, the velocity ratio

(v_r) is taken to be the ratio of the predicted velocity relative to the velocity predicted by Miller's model. Figure 4.1 presents the trend in deflection and the relative relationship between the study's model and Miller's relation. At a velocity ratio of unity, the plate collapses; confirming the analogous outcome between the outcome predicted by Miller, and the outcome predicted by the study's model after having removed all non-recoverable fluid losses. In theory, the relative deflection shown in Figure 4.1 would ideally be null below Miller's velocity and unity above it. The difference in the value on the left side is a result of the iterative solver's tolerance. Had the tolerance been smaller, the final solution would have been smaller. However, tolerance was left at a relatively large value to demonstrate the robustness of the model and its ability to yield a representative solution regardless of the iterative solver's convergence criterion.

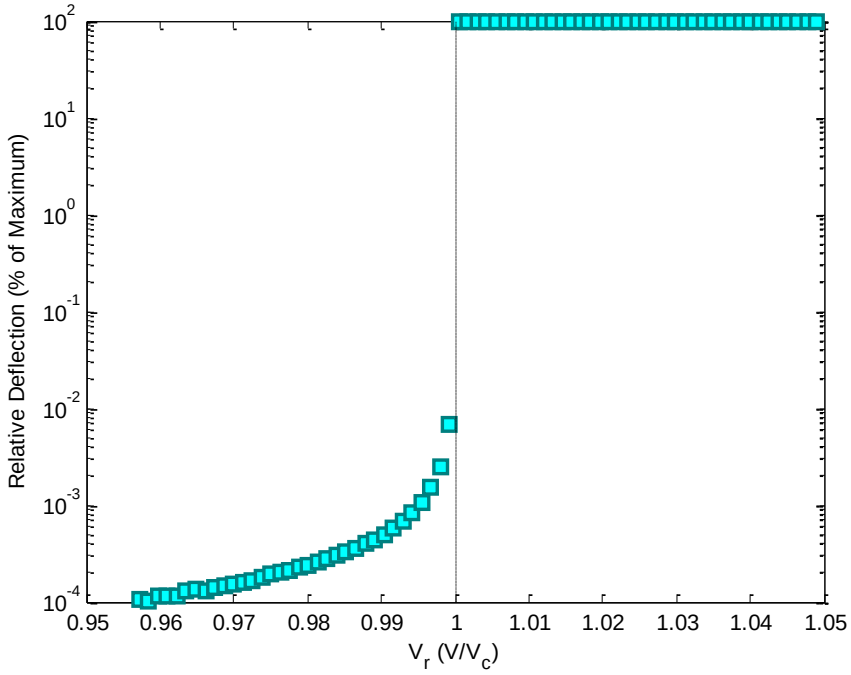

Figure 4.1: Model prediction of plate collapse relative to Miller's model

One of the most sensitive individual parameters within the model is the form loss characterization and quantification at the inlet of each flow channel, which ultimately

yields the pressure difference between the two adjacent channels; sensitivity of deflection to form loss has been analytically shown to hold true by Kane [3]. The form loss coefficient values (*k*), fluid velocities, initial and final pressure differential, and pressure drop were recorded for a 4 m/s inlet flow. Results are tabulated in Table 4.2, and the spanwise-centerline deflection for each scaling method is plotted along the axial length of the plate in Figure 4.2.

Table 4.2: Parameters associated with potential values for k

Parameter [Symbol] (unit)	D_n^2/D_3^2	A_n/A_3	$D_n^2/D_3'^2$	A_n/A_3'
Channel 1 inlet form loss coefficient [$k_{1,in}$] (#)	0.3616	0.2693	0.05837	0.02869
Channel 1 outlet form loss coefficient [$k_{1,out}$] (#)	0.7548	0.4153	0.06508	0.01215
Channel 2 inlet form loss coefficient [$k_{2,in}$] (#)	0.3208	0.2207	0.1652	0.09611
Channel 2 outlet form loss coefficient [$k_{2,out}$] (#)	0.5678	0.2727	0.1067	0.04094
Channel 1 superficial velocity [v_1] (m/s)	4.643	4.602	4.704	4.647
Channel 2 superficial velocity [v_2] (m/s)	4.906	4.932	4.864	4.902
Plate load at inlet [*w*] (Pa)	-5220	-4885	-5708	-5249
Plate load at outlet [*w*] (Pa)	-4081	-4236	-637.5	-2071
Total pressure drop across plate [Δp] (Pa)	50290	45510	41720	40300

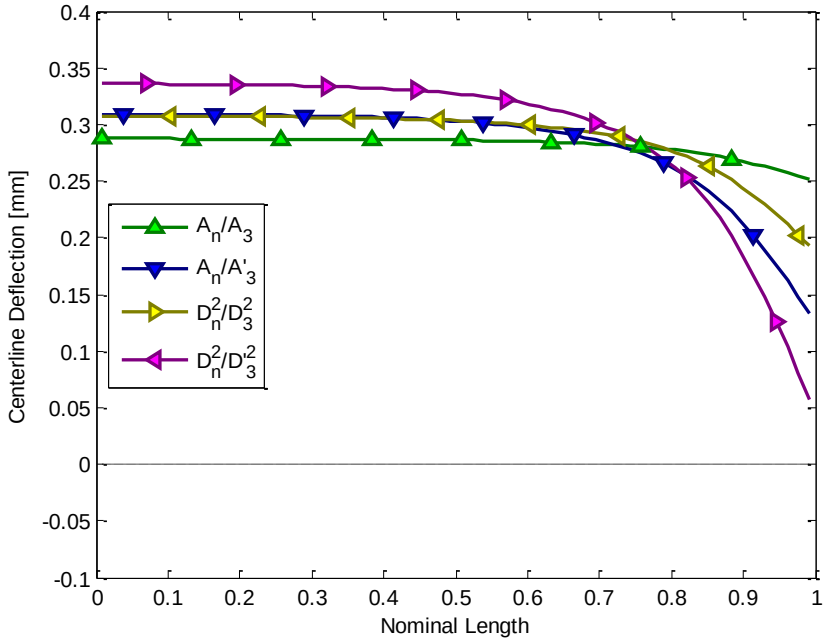

Figure 4.2: Axial deflection profile with varying entrance and exit loss terms

It can be seen from Figure 4.2 application of the area driven form losses as opposed to the hydraulic diameter results in a generally smaller deflection. Note, for high-aspect ratios, the area is proportional to the hydraulic diameter. Consequently, squaring the difference term within the of the minor loss coefficient relation results in a large minor loss ergo, a larger deflection difference. Use of the 'perceived area' or 'perceived diameter' resulted in a larger deflection. Using the perceived area or diameter (A', D') caused the minor loss terms to be greatly reduced as would be expected. The unexpected result was an increase in plate deflection. As the ratios approach unity, the influence of the minor loss terms at the inlet yielded a larger difference. Conversely, the minor loss terms at the outlet tended to yield a similar solution. In essence, a larger difference in pressure at the leading edge of the plate resulted in a smaller difference in pressure at the outlet. For the purposes of the combined fluid-structure solver, the A' scaling as derived in equation (29) was utilized. It was chosen because it has been shown, in previously conducted studies, to generally function appropriately as the form loss distribution relation associated with parallel plate arrays [6].

4.2 Quasi-Verification of Structural Solver

Perhaps the boldest assumption in developing the model detailed herein is the plate is represented by a wide beam profile across the spanwise direction (perpendicular to the flow direction) along the entire length. To support the verification of the model's structural computation and modeling ability, it was compared with ABAQUS models under two different loading profiles. First, the pressure as a function of *y* (prior to the addition of the acceleration terms) was approximated for a 6 m/s inlet flow velocity. The pressure profile was modeled by a hexatic polynomial to ensure consistency in ABAQUS. The hexatic polynomial was also used in developing the deflection profile of the code. Second, a uniform pressure distribution was used for further comparison. The pressure load profiles used to compare ABAQUS to the code are presented in Figure 4.3.

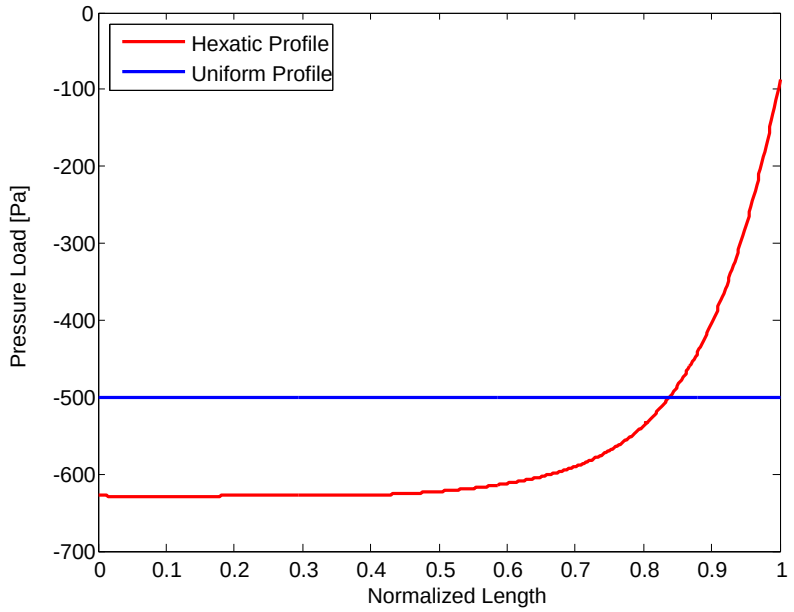

Figure 4.3: Axial pressure profiles utilized for model verification

4.2.1 Assessment of the Wide Beam Assumption

Both of the two pressure profiles were applied to ABAQUS and the structural solver detailed herein. Additionally, each profile was compared while considering three edge

boundary condition combinations. In all cases, the long plate edges (along the axial length of the plate) were assumed to be clamped, while the leading and trailing edges were varied, with free-free (FF), pinned-pinned (PP), and clamped-clamped (CC) boundary conditions. For the two pressure loadings chosen, along with the three applied end conditions, the profile shape from ABAQUS was compared to a wide beam profile. The average deflection of a wide-beam under a given loading condition can be obtained by integrating

$$z = \frac{w}{24D} x^2 (b-x)^2 \tag{35}$$

with respect to *z*, over the width, and subsequently dividing by the width of the plate. Performing said operations results in

$$\bar{z} = \frac{w}{720D} b^4, \tag{36}$$

the average deflection. If the average deflection of the plate is known at any given *y* location, the "wide-beam" profile shape may be determined from the mean deflection of the plate. Combining equation (36) with equation (35) achieves the ideal profile shape in terms of the actual profile shape's mean deflection. The relationship between the deflection and average deflection,

$$z = \frac{30\bar{z}}{b^4} x^2 \left(b-x\right)^2, \tag{37}$$

for a wide beam may be utilized to determine the relative error between the expected plate deflection (determined by ABAQUS) and the optimal deflection achieved by the code. The deviation from the ideal profile,

$$\overline{\Delta z} = \frac{\sum_{i=1}^{N} \left| z_{i_{ideal}} - z_{i_{actual}} \right|}{N}, \tag{38}$$

may be used to compare how well the actual plate profile shape fits the ideal or wide-beam model utilized in the code. Alternatively, it may be compared as a percentage by dividing by the absolute value of the average deflection. The results of the optimal profile

comparison may be seen for both pressure profiles and all three end conditions from Figure 4.4.

For all cases presented in Figure 4.4, the solution form yielded from the model results in a solution nearly analogous to the ABAQUS solution within the middle region of the plate, while it diverges from the ABAQUS solution at the leading and trailing edges. Deviation near the edges is understood to be a causal effect of the application of wide-beam-theory within the structural domain of the model. The flexural rigidity of the plate is well understood and characterized via the wide-beam relation shown in (35); however, when the cross-product stress-tensors, within the plate equation shown in (26), become more influential toward the plate's response to a hydraulic load, the model's ideal solution begins to diverge from the ABAQUS solution. Note, however, the largest percent deviation between the model and the ABAQUS solution was found to be approximately ten percent with most cases yielding a maximum percent deviation of approximately four percent. Within Figure 4.5 three variants of the study's model are presented along with the ABAQUS solution. Figure 4.5 presents plate deflections with leading and trailing edges free (a-e), pinned (f-k), and clamped (l-o); given a uniform load (a,b,f-h,l,m) and hexatic load(c-e,i-k,n,o); and using ABAQUS (a,c,f,i,l,n), the base model (b,d), the spring model (e,g,j), and the additional term model (h,k,m,o) These variants are referred to as the 'base model' an 'added term model' and a 'spring model'. Each model variant has been detailed in section 3.5 .

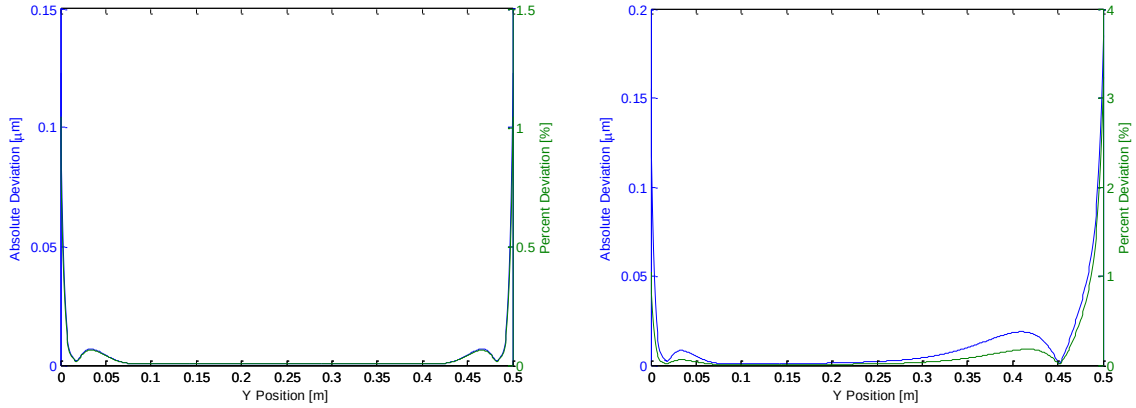

(a)

(b)

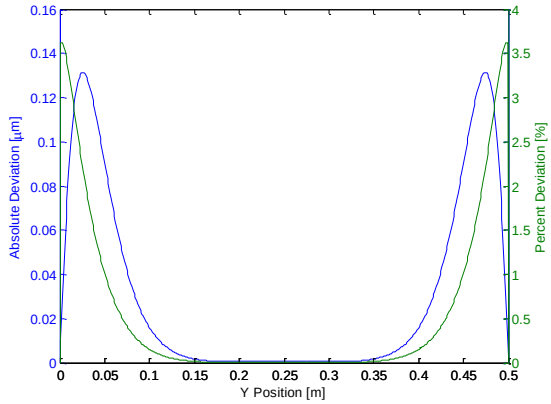

(c)

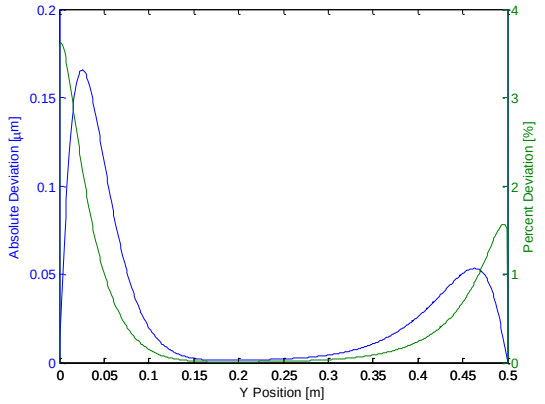

(d)

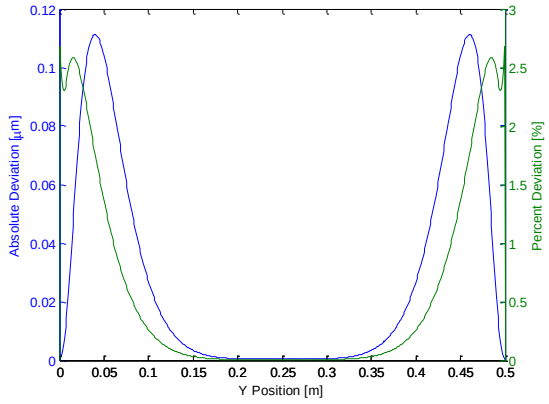

(e)

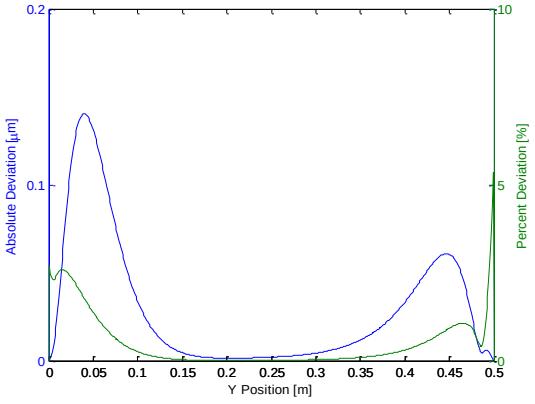

(f)

Figure 4.4: ABAQUS deviation from the ideal wide-beam profile with leading and trailing edges free (a-b), pinned (c-d), and clamped (e-f), given a uniform load (a,c,e) and Hexatic load (b,d,f) along the axial plate length

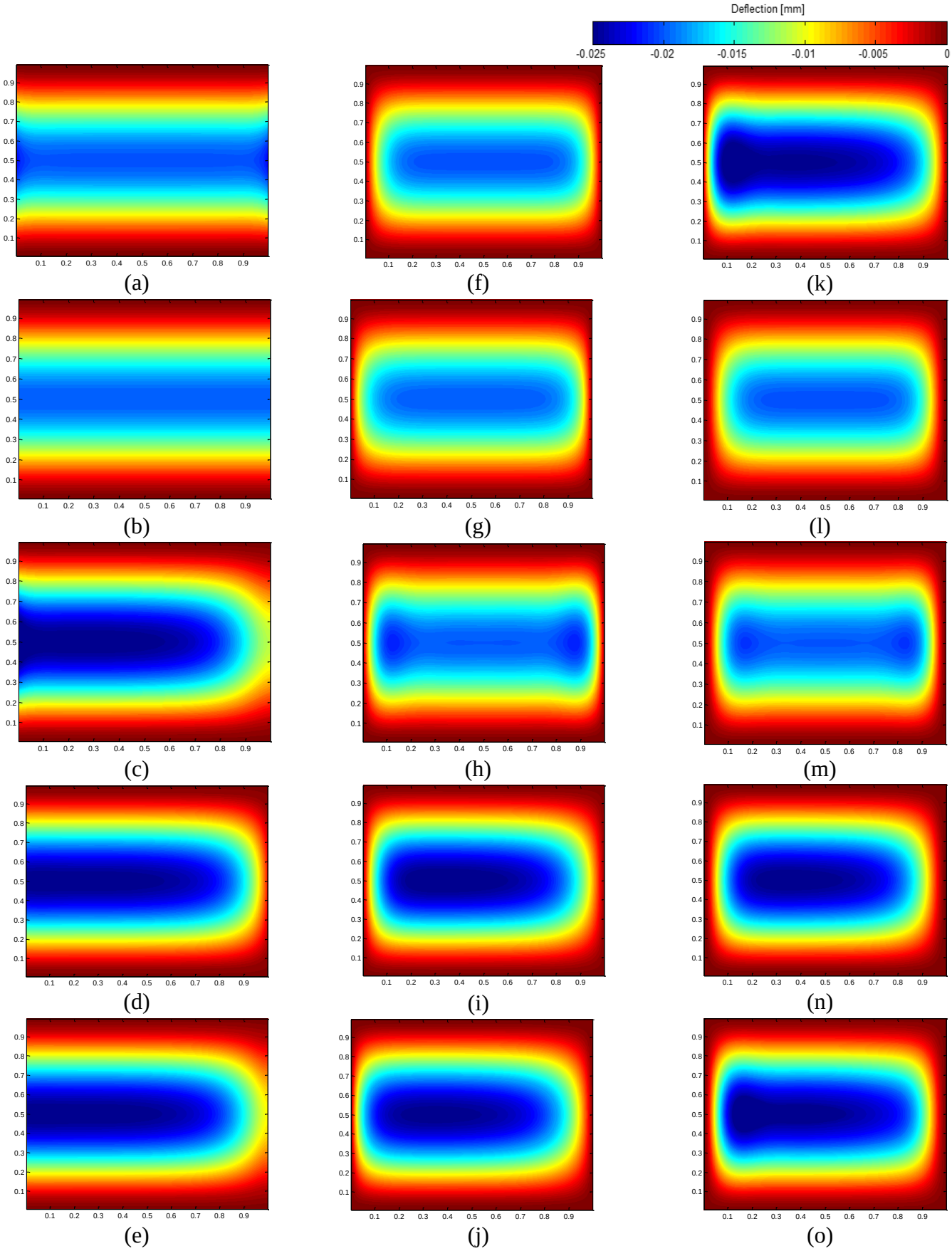

Figure 4.5: Plate deflections

Figure 4.6 presents the axial deflection profile taken along the spanwise centerline of the plate for all applicable models for each of the three edge boundary condition cases. Of the three model variants, the ‘spring model’ yielded the most agreeable deflection profile relative to ABAQUS, and was therefore selected for further application within the study.

In an attempt to further characterize deviation of the ‘spring model’ relative to the ABAQUS solution, a complete contour presentation of the explicit deviation is shown in Figure 4.7. Figure 4.7 provides a graphical representation of the relative deviation of the solution domain for the ‘spring model’ given a uniform load and Hexatic load, as compared to the ABAQUS solution. Note, the largest deviations tend to occur near the leading and trailing edges of the plate for all boundary condition sets. The large deviation is in agreement with the observations made from the ‘ideal model’ in Figure 4.4.

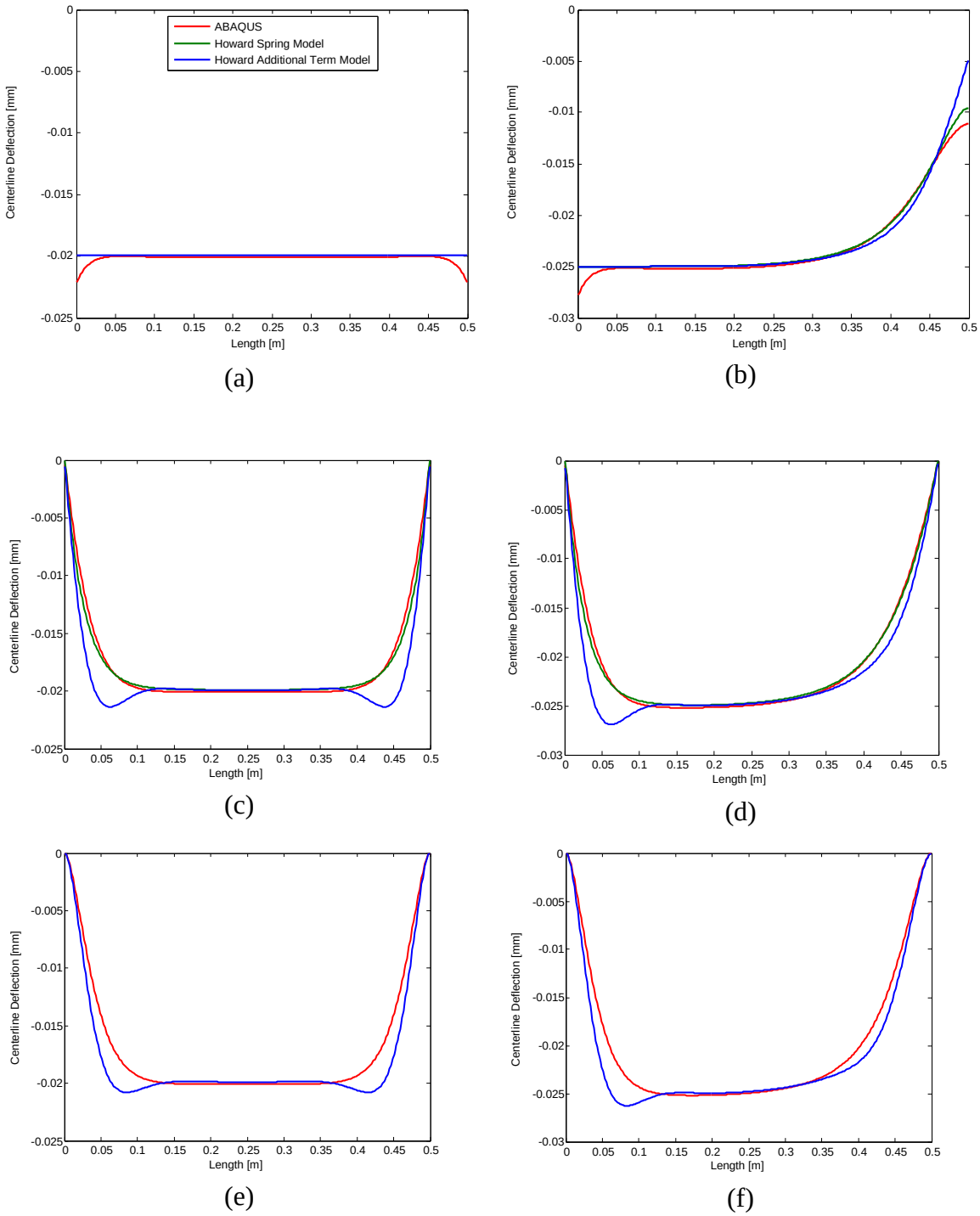

Figure 4.6: Plate deflection profile
with leading and trailing edges free (a-b), pinned (c-d), and clamped (e-f), given a uniform load (a,c,e) and hexatic load (b,d,f) along the axial plate length with ABAQUS results in red, the standard code in blue, and spring model in green (a,b,c,d only)

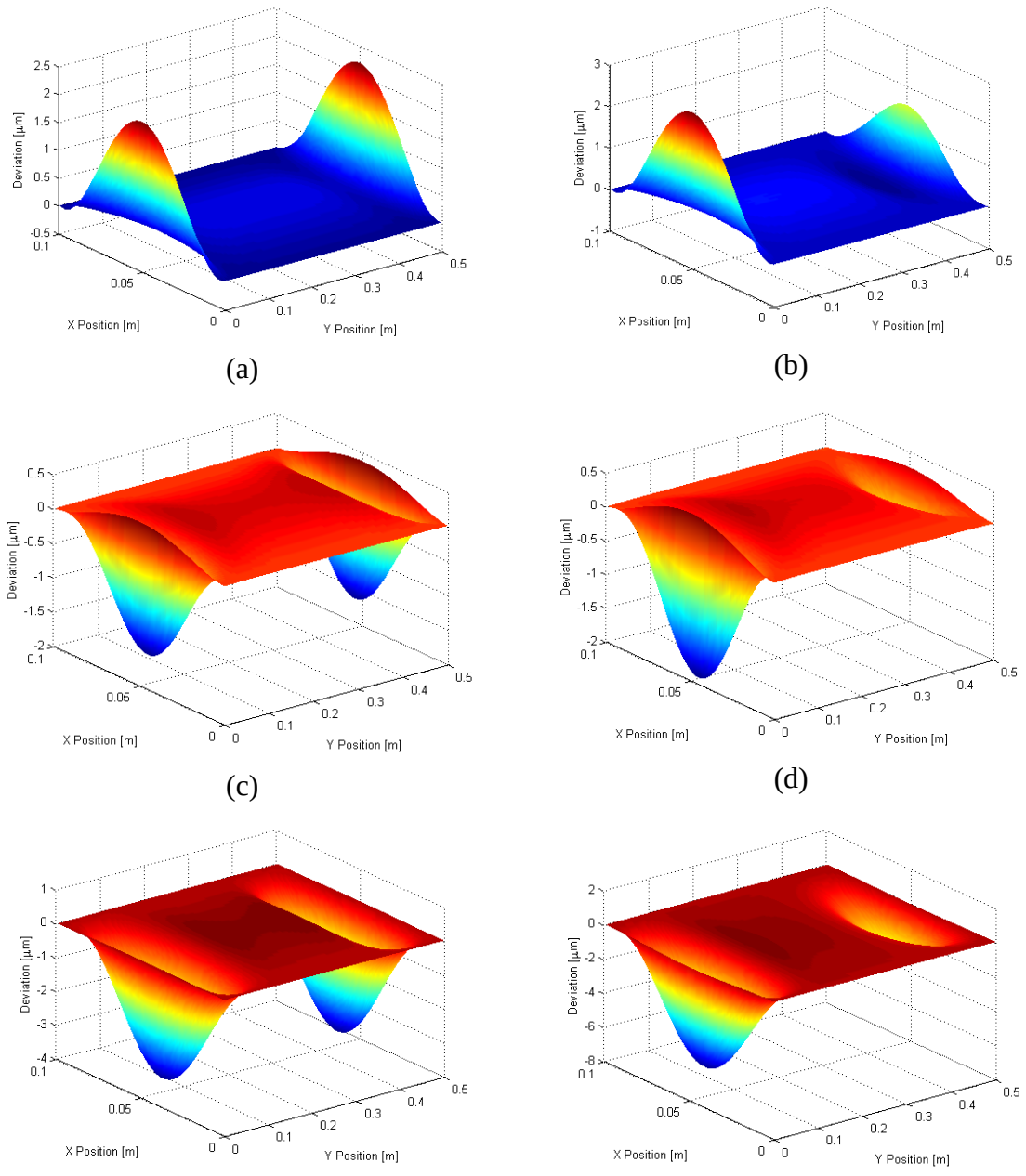

Figure 4.7: Deflection deviation
of spring model (a-d) and full term model (e-f) relative to ABAQUS solution with leading and trailing edges free (a-b), pinned (c-d), and clamped (e-f), given a uniform load (a,c,e) and hexatic load (b,d,f) along the axial plate length

In addition to the graphical representation of the deviation for spring model shown in Figure 4.7, Table 4.3 provides a summary of the maximum relative deviation between the model's solution for each model and the ABAQUS solution, considering all load types and boundary condition sets. Table 4.3 further demonstrates, the spring model, while not always yielding the smallest maximum relative deviation to ABAQUS in all cases, in general, generates a credible and reproducible solution and is, therefore, recommended for application under similar conditions over the alternate forms.

Table 4.3: Maximum deviation of model relative to ABAQUS

Load Type	Model deviation from ABAQUS	Leading and trailing edge boundary conditions [μm deviation] and (% deviation)		
		FF	SS	CC
Uniform	Base Model	2.1890 (9.914)	---	---
	Spring Model	2.1890 (9.914)	-1.5821 (-15.24)	---
	Added Term	2.1890 (9.914)	-4.9734 (-33.71)	-3.6176 (-24.82)
Hexatic	Base Model	7.3333 (66.047)	---	---
	Spring Model	2.7579 (13.771)	-1.9873 (-17.934)	---
	Added Term	6.1669 (55.565)	-6.296 (-36.636)	-4.7717 (-26.016)

4.3 Comparison to Single Plate Experimental Data

A series of experiments were conducted at the University of Missouri, Columbia mapping a single plate's structural response to a variety of fluid boundary conditions. In the experiments, a single aluminum plate was placed in a Plexiglas test section and positioned so two flow channels were adjacent to the plate, one of which was larger in thickness than its partner. During the conduct of the experimental study, the test plate was clamped along its axial length, while two sets of conditions were applied to the leading and trailing edge. In one case, the leading and trailing edges were left free, and in the second they were pinned using a removable pin at the midpoint designed to replicate the

boundary condition of a comb [1]. A summary of the input parameters used to model the experiment are presented in Table 4.4.

Table 4.4: Parameters used for analysis of a single plate

Parameter (Symbol) [units]	Value
Plate length [l] (m)	0.6477
Plate width [b] (m)	0.1102868
Plate thickness [a] (m)	0.0009652
Young's modulus [E] (GPa)	70
Poisson's ratio [υ] (#)	0.33
Flow channel 1 height [h_1] (m)	0.002032
Flow channel 2 height [h_2] (m)	0.002540
Inlet and outlet flow channel height [h_3] (m)	0.0056204
Density [ρ] (kg/m^3)	997
Viscosity [μ] (Pa-s)	0.00088871
Surface roughness [ε] (m)	0.0000015
Spring constant [λ] (MN/m)	300

A thorough characterization of the experimental configuration was conducted by the investigators of the experimental study. While in theory each flow channel would be perfectly flat, some variance of the channel spacing occurred in both *x* and *y* directions. For each respective boundary condition set in the experiment, a computation is conducted using the 'ideal' flat plate geometry and the measured 'as-built' geometry documented by the experimental investigators [1]. The comparison was made to determine the influence of small deviations in geometry, as well as the model's ability to capture a more representative solution when considering the as-built conditions of the experiment. A graphical representation of the ideal geometry and the as-built geometry is shown in Figure 4.8.

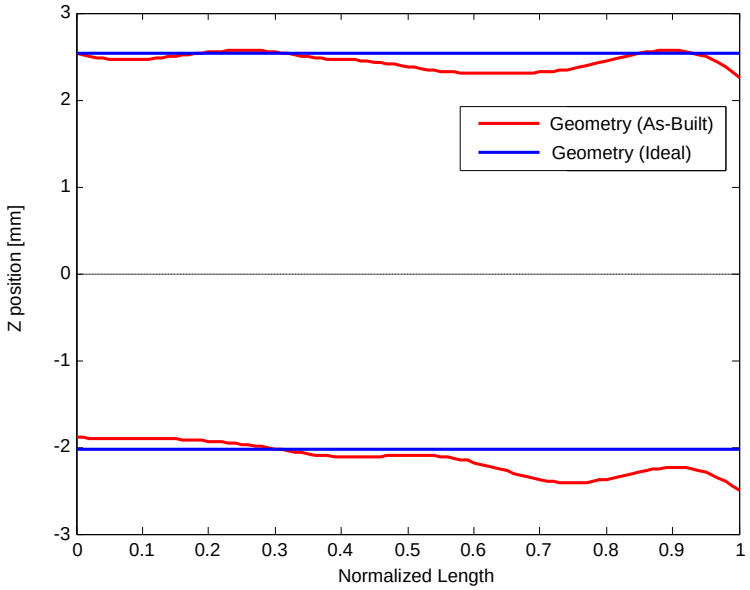

Figure 4.8. Comparison of channels for ideal and as-built geometries

The deflection profile along the axial length of the plate located at the plate's spanwise centerline is presented in Figure 4.9 for each model using the 'spring model' and is compared against the experimental data. Note, all experimental data presented herein is accompanied with error bars representing 95 percent confidence. Figure 4.9 (a) and (b) present the deflection profile corresponding to a flow rate of 1 kg/s; Figure 4.9 (c) and (d) correspond to a flow rate of approximately 2.25 kg/s; and Figure 4.9 (e) and (f) correspond to a flow rate of approximately 3.5 kg/s. The profile shapes compare well with the experimental results obtained. The largest discrepancy is observed to occur with the free plate at high velocities. There is a striking difference between the 'ideal' and 'as-built' results. The absolute difference in channel height is greater in the ideal case, yet the deflections remain significantly smaller.

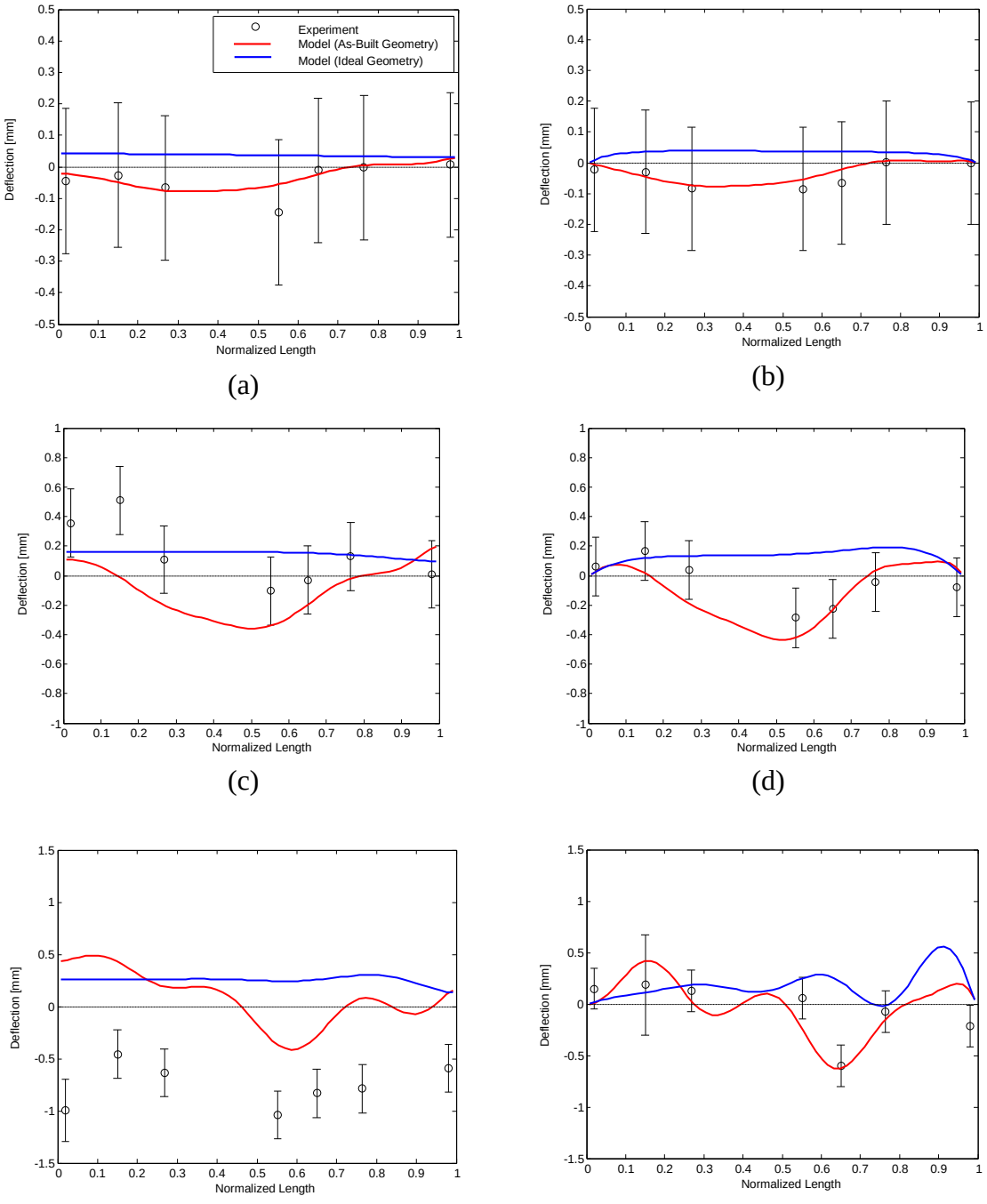

Figure 4.9: Deflection profile comparisons
for ideal and as-built channel geometries with leading and trailing edges free (a,c,e) and pinned (b,d,f), for low (a,b), medium (c,d), and high (e,f) flow rates

Despite having the maximum deflection in the opposite direction for the free-free case, the plate profiles were remarkably similar with exception of the ends of the plate. The biasing in deflection toward the lower flow channel for the ‘as-built’ geometry was seen similar to the experiment. The difference between deflection magnitudes of the experiment and computational solution became significantly larger at higher flow rates for the free-free case. The most likely cause for the inversion and lack of magnitude comes from the lack of additional deflection at the end of the plate which was witnessed Figure 4.7. At each of the plate ends, the minor loss term is determined; therefore any additional deflection results in a significant impact on the overall flow field. Additionally, the extra deflection would result in a significantly different acceleration term. If such is the case, one would expect the pinned-pinned conditions to be much more representative, which is, in fact, seen in Figure 4.9 (b), (d), and (f).

Lastly, a comparison is made between the maximum plate deflection experimentally observed and the simulation results for the ideal and as-built conditions for both sets of leading and trailing edge boundary conditions. Figure 4.10 and Figure 4.11 summarize the comparison. Notice the relatively uniform and predictable trend of the ideal model, whereas the as-built model tends to exhibit a number of traits which are seen to be present in the experimental data.

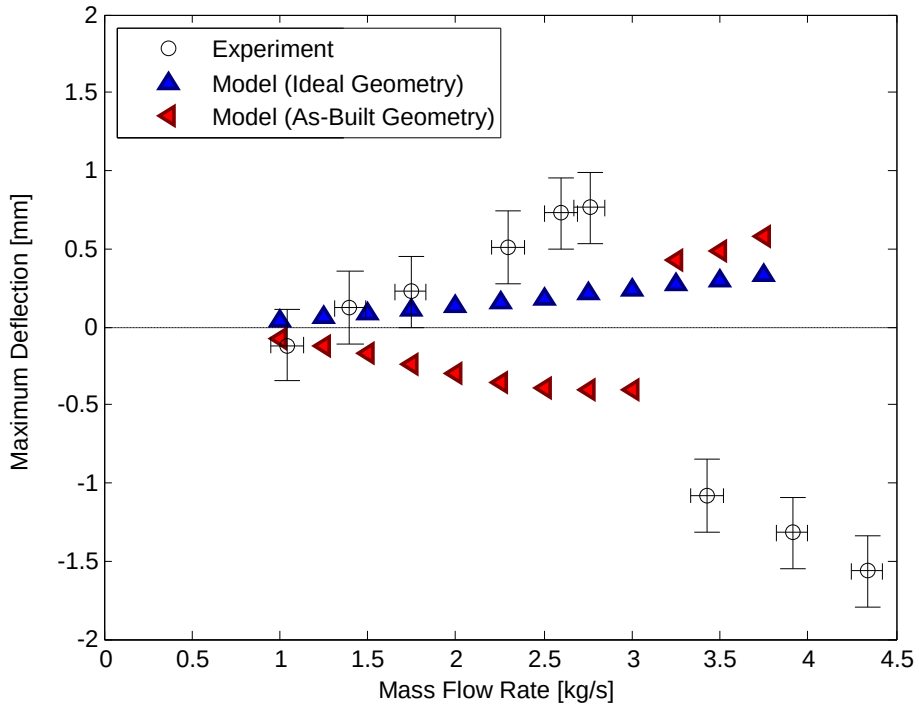

Figure 4.10: Maximum plate deflection for leading and trailing edges free

Considering the boundary condition where leading and trailing edges are free, a “snap” is observed around a flow rate of 3 kg/s for the experiment. The numerical simulation also exhibits a “snap-like” effect at the same flow rate. The dynamic response of the ‘snap’ of the plate was not instantaneous within the computational model’s solution development as it is predicted to be from the experiment pressure data. For the ideal geometry, the critical flow rate is 2.86 kg/s, per equation (6), which is approximately the flow rate of the plate snap during the experiment. The critical flow value is between the medium and high flow rates in Figure 4.9, lending to a further understanding as to why the axial profile of the plate within the simulation tended to exhibit a profile which would be perceived as a buckled shape. For the ideal results no snap occurred; however, significant distortions of the plate began to occur around the critical flow rate as predicted by Miller.

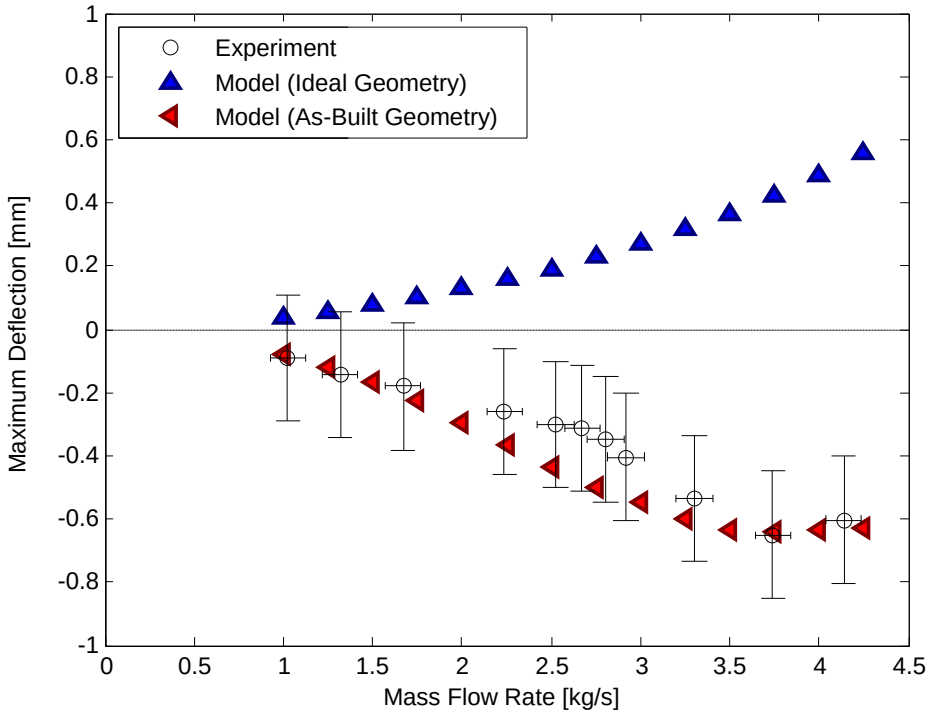

Figure 4.11: Maximum plate deflection for leading and trailing edges pinned

Furthermore, from Figure 4.11, one can clearly see alignment of the as-built model's maximum deflection as compared to the experimental results through the entire flow rate range. If one were interested in acquiring a relatively comprehensive solution or a plate having two edges clamped and two edges pinned, the model presented herein would lend a solution both effective in predictive capability and economic.

A final note should be made regarding flutter in the plates. From equation (11), a reduced velocity of 20 (the expected value of flutter) corresponds to a flow rate of 4.27 kg/s. Above the flutter flow rate, both the free-free and pinned-pinned simulations were unstable. Since the simulation was searching for a steady solution, any flutter characteristics resulted in the solution not converging. In the case of pinned-pinned plate, the solution achieved a convergence slightly higher than the free-free plate. Since the

plate was pinned, the boundary conditions at the inlet and exit were forced resulting in a postponement of flutter driven by changes in the minor losses.

4.4 Comparison to Six Plate Experimental Data

After a comparison for the two dimensional model, an additional analysis was performed using the GTPA geometry. The plate model was designed for use with multiple plates for which the GTPA has six. An important feature of the GTPA is the inclusion of a comb which pins the plates at the axial ends (shown in Figure 4.12). The comb creates additional frictional losses which creates a significant difference in the pressure load profile. The combs at the ends effectively reduce then increase the hydraulic diameter of the plate and provide additional expansion and contraction terms. As a result, the pressure profiles generated off of the hydraulic diameter assumption and the CFD model presented by Roth [8] were significantly different.

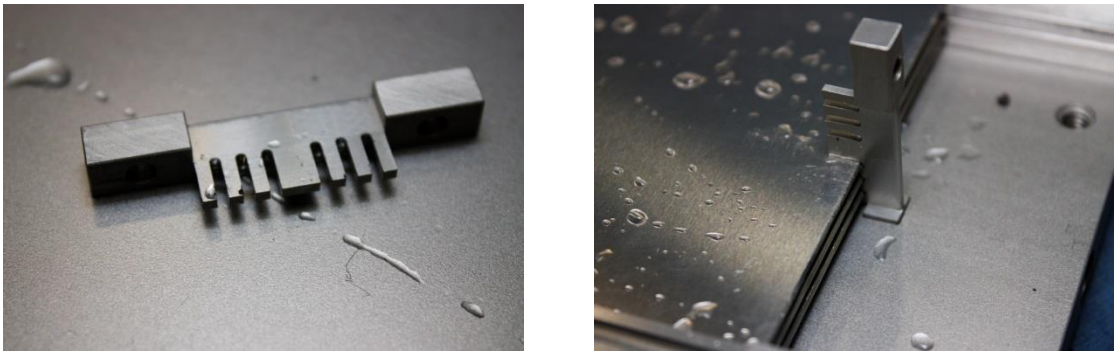

(a) (b)

Figure 4.12. The comb pulled out (a) and inserted in the GTPA (b)

To achieve a representative solution for comparison with experimental data, the minor loss coefficients were calculated from the CFD simulations [8] using equation (34) and combined with the aforementioned component of the minor loss term. The properties of the plate as well as the coefficients used are listed in Table 4.5.

Table 4.5: Parameters used for the GTPA

Parameter (Symbol) [units]	Value
Plate length [l] (m)	0.6096
Plate width [b] (m)	0.0889
Plate thickness [a] (m)	0.00127
Young's modulus [E] (GPa)	70
Poisson's ratio [υ] (#)	0.33
Flow center channel height [h_1] (m)	0.002032
Flow peripheral channel height [h_2] (m)	0.002540
Inlet and outlet flow channel height [h_3] (m)	0.02225
Density [ρ] (kg/m^3)	990
Viscosity [μ] (Pa-s)	0.000553
Surface roughness [ε] (m)	0.0000015
Spring constant [λ] (MN/m)	300
Minor Loss Coefficient [k_{in}], CFD (Inlet)	0.6
Minor Loss Coefficient [k_{out}], CFD (Outlet)	1.6

In Table 4.5, two new values for minor loss coefficients are introduced. The values were designed to more appropriately reflect the physics of the GTPA. In the case of the two plate channel, the minor loss terms are similar, however, in the case of the GTPA it can be expected the minor loss terms will be different in the outer channels when compared to the central channels, due, in part, to the differences in acceleration of the fluid. The outer channels maintain a wall boundary condition while the central channels use fluid traveling at approximately a uniform velocity. The CFD model included the pins shown in Figure 4.12. The values for the minor loss coefficients were derived from the pressure data presented in Roth's case 1 which had a flow rate of 11 kg/s [8]. Two minor loss term cases were considered; one using Equation (29) to determine the pressure drop across the test section and another using the minor loss values stated in Table 4.5. It is important to look at potential differences in the profile stemming from changes in the minor loss coefficient. For the rigid hydraulic plate conditions, the ideal GTPA geometry was used to compared the plate deflection profile for the minor loss values listed in Table 4.5 and derived from Equation (29). The profiles can be seen in Figure 4.13.

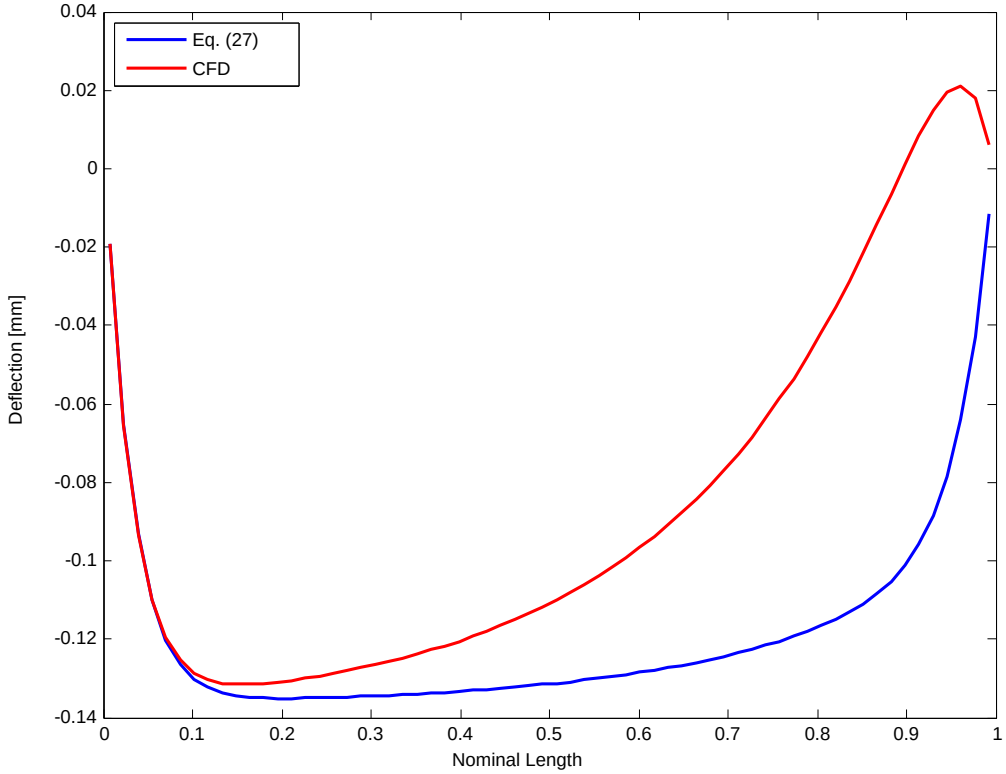

Figure 4.13: Mean deflection profile at 12 kg/s comparison with rigid hydraulic plates.

Figure 4.13 shows the comparisons of the average deflection at each *y*-position using the values. While the maximum deflection is comparable, the profiles are slightly different. The larger minor loss coefficients derived from the CFD model produce additional upward bending of the plate, whereas the equation based value for the minor loss coefficient pushes the plate entirely into the channel below. The large loss coefficients which could result from the pin, strain gauges, or the pitot tubes could be better represented by the CFD derived form loss coefficient.

While the deflection profile provides some insight as to the effect the minor loss term has on the plate deflections, it doesn't directly indicate which minor loss term is better suited for use in the computational model. To determine the better minor loss coefficient, the pressure drop through the assembly was compared for a rigid geometry identical to CFD

model presented by Roth, and a real geometry, or "As-Built" GTPA geometry with flexible plates and strain gauges within a channel. The results of the comparison are shown in Table 4.6.

Table 4.6: Pressure Drop Data

Data Set	Total Pressure Drop at (Pa)
Experimental GTPA (8.43 kg/s)	51.71 kPa
CFD Model (11.2 kg/s) [rigid]	175.8 kPa
Computational Model (8.43 kg/s) {form loss coefficient from Equation (29)}	50.12 kPa
Computational Model (8.43 kg/s) {form loss coefficient from Table 4.5}	83.87 kPa
Computational Model (11.2 kg/s) [rigid] {form loss coefficient from Equation (29)}	128.58 kPa
Computational Model (11.2 kg/s) [rigid] {form loss coefficient from Table 4.5}	202.7 kPa

Table 4.6 presents the pressure drop across the test section for the two minor loss conditions previously stated. Despite being tabulated from the CFD model, the minor loss values that were calculated created a larger pressure drop than was seen in the model. The larger pressure drop is likely caused by the difference in minor loss terms between the outer and central channels. The form loss coefficient was averaged for the central three channels as opposed to being directly calculated for every channel. The minor loss term is geometry dependent which resulted in a higher pressure drop when a constant form loss coefficient was used. Alternatively, the equation derived values for the pressure drop resulted in a pressure drop that was nearly 2/3 of the expected value. The best overall agreement, however, was between the experimental data and the minor loss terms derived from Equation (29). Consequently, the minor loss terms derived from Equation (29) were used to determine the deflection profiles in the GTPA experiment. Since one data point is hardly sufficient, the complete experimentally measured pressure drop data was compared to the model's pressure drop results in Figure 4.14.

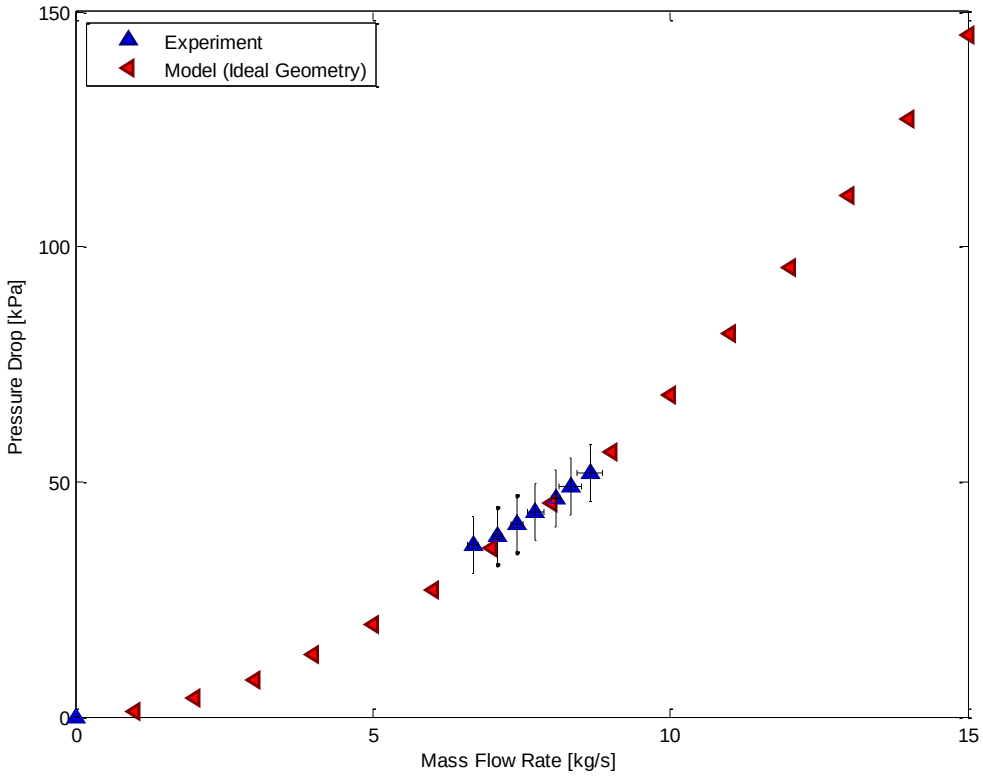

Figure 4.14: Pressure drop comparison between model and experiment.

The pressure drop data of the as-built model compares very well between the model and the experiment as can be seen in Figure 4.14. The range of the model extends well beyond the experiment; however, the results are comparable for the test range. The pressure drop across over the model exhibits a near quadratic trend as is seen in experiments and expected from the values presented in equation (14).

4.5 Miller's Critical Velocity and Stability

For the GTPA boundary conditions, the value for Miller's critical velocity is 8.62 m/s (~11 kg/s) for the small gap parallel plate region. A significant instability in the ideal model occurred at the corresponding flow rate as was witnessed in the one plate study.

The primary difference between the single plate and multi-plate models is small increases in the mass flow rate requiring large decreases in the relaxation factor to achieve quasi-stability. The largest flow rate achieved was 12 kg/s. When the as-built model was used, the solution maintained stability up to about 15 kg/s. Because the as-built model deviates from the ideal situation, there is less room to deviate from an expected profile. As such, the as-built model ends up being more robust than the ideal one for the case of six plates. Additionally, the lack of stability in the six plate model is more apparent than the two plate model because of the number equations involved.

4.6 Comparison to Experimental Data

The experimental data that quantifies the Test Plate's deformation was obtained through the use of a channel gap probe (CGP). The CGP measured the gaps between the plates before and after testing. While the plate deflection values can't be directly obtained (except on the hydraulic plates furthest from the center) the gap size before, after, and change can be measured. While it is important to note the change is caused by a plastic deformation, and the model cannot quantify plasticity, the general profiles may still be compared to one another to confirm trends.

A model of the GTPA under the influence of flow can be seen in Figure 4.15. The as-built GTPA has a few larger differences than the ideal model. The most notable is the presence of strain gauges. The strain gauges are integrated into the plate model and provide a reduction in the overall gap thickness where they are located. The strain gauges are included by reducing the gap size only. They do not increase the stiffness of the plate or add additional frictional losses within the model.

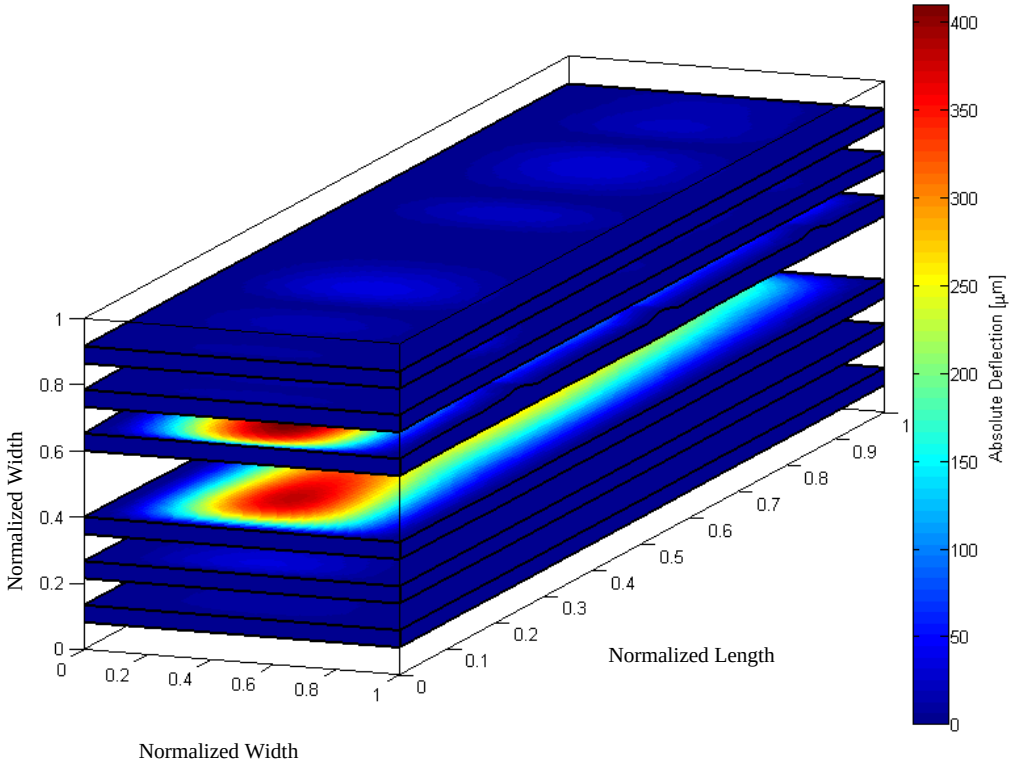

Figure 4.15: Model geometry and plate deflections

Figure 4.15 shows the deflection locations, relative magnitude of the deflections and general geometry of the plates at a flow rate of 12 m/s. The values of deflection can be seen to be largest in the central channel and deflect towards the center of the plate. The larges deflections are at the front end of the plate and taper off towards the back end. An alternate presentation of the deflections experienced by the plate can be seen in Figure 4.16 and Figure 4.17.

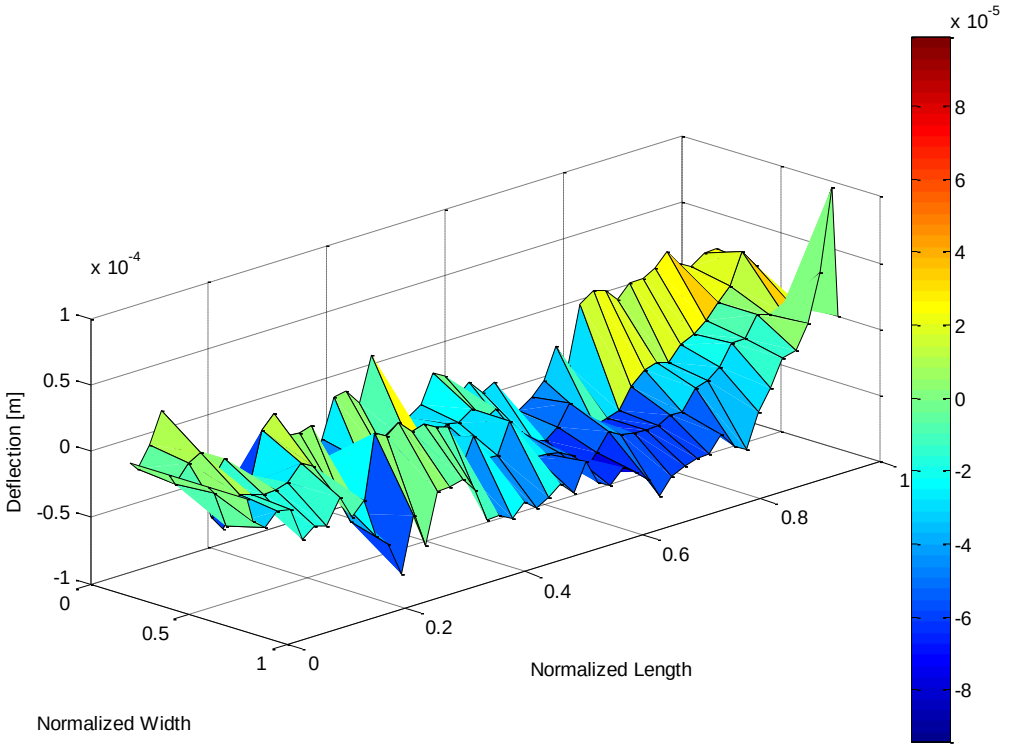

Figure 4.16: GTPA measured test plate deflection

Figure 4.16 shows the deflection of the test plate as measured after the test. This is done to show the relative magnitudes of the deflections seen in the plate. A profile comparison with the model results can be seen in Figure 4.18.

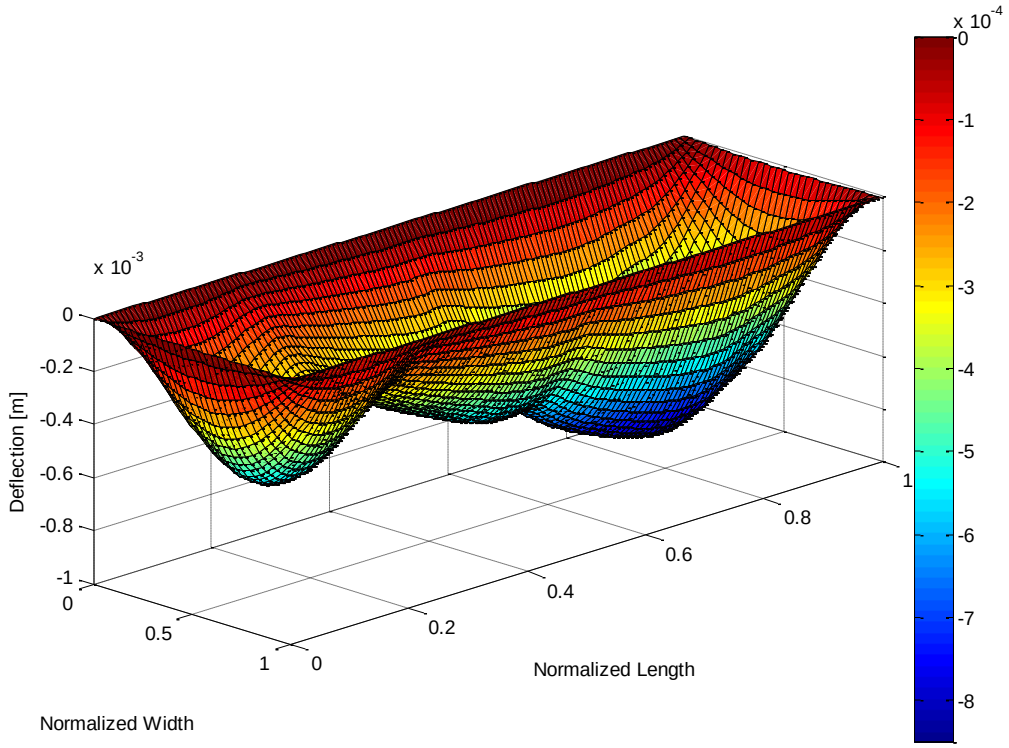

Figure 4.17 GTPA deflection from as-built computer model at 8.43 kg/s

Figure 4.17 shows the deflection profile of the test plate obtained from the as-built computer model. The deflection shows the test plate deflection largely toward the center channel with the largest deflections occurring about three quarters from the inlet.

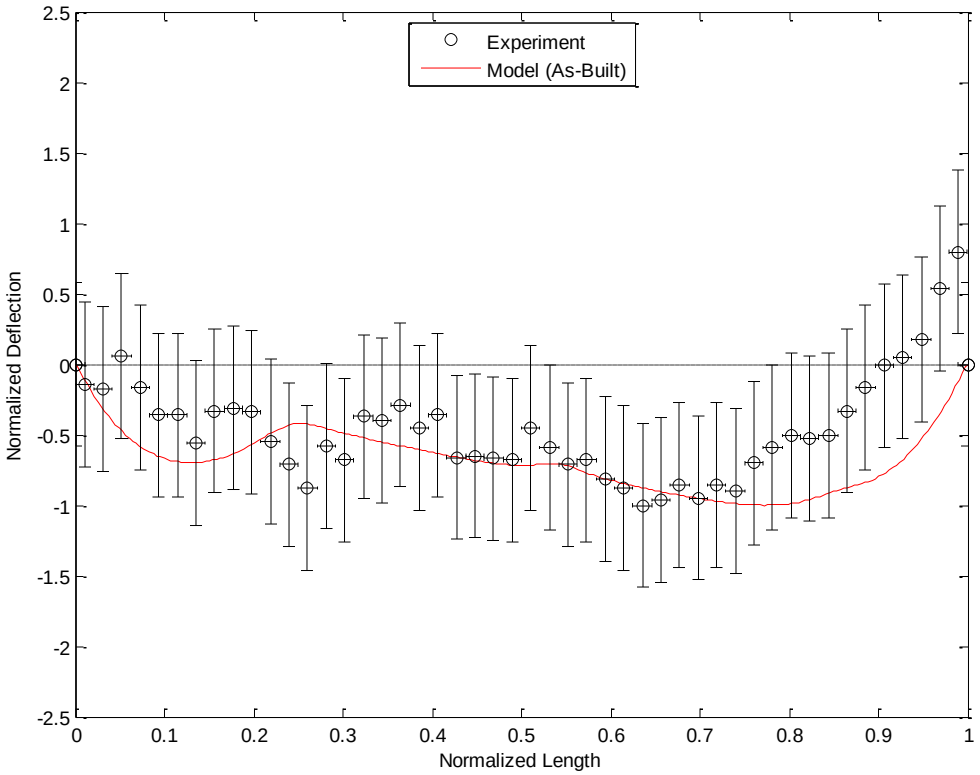

Figure 4.18: Test plate axial deflection profile

Figure 4.18 shows the normalized deflection of the as-built model test plate profile at 8.43 kg/s compared alongside the experimental results. The plate and model profile share the same general trends. The biggest difference is seen in at the back end of the plate. The difference in form loss coefficients as witnessed in Figure 4.13 may be seen as an explanation for the difference. The data being presented is post test data. As a result all deflections are caused by plastic deformations. Since the model doesn't include plastic deformations, the unloaded plate may look very different than the one experiencing a fluid load.

4.7 Hastalloy vs. Aluminum Boundary Conditions

Due to the desire to create more stringent boundary conditions, the typically flexible aluminum side plates were replaced with a more rigid Inconel boundary condition. For the following cases, the effect of the Inconel boundary is modeled by forcing all deflections in the plate to null. While this is not realistic, a null net deflection is very reasonable; especially considering the flexural rigidity of the Inconel is an order of magnitude greater than aluminum. Changing the boundary conditions of the GTPA is likely to affect the deflection profile and magnitude of the test plate. The nature of this impact is seen in Figure 4.19.

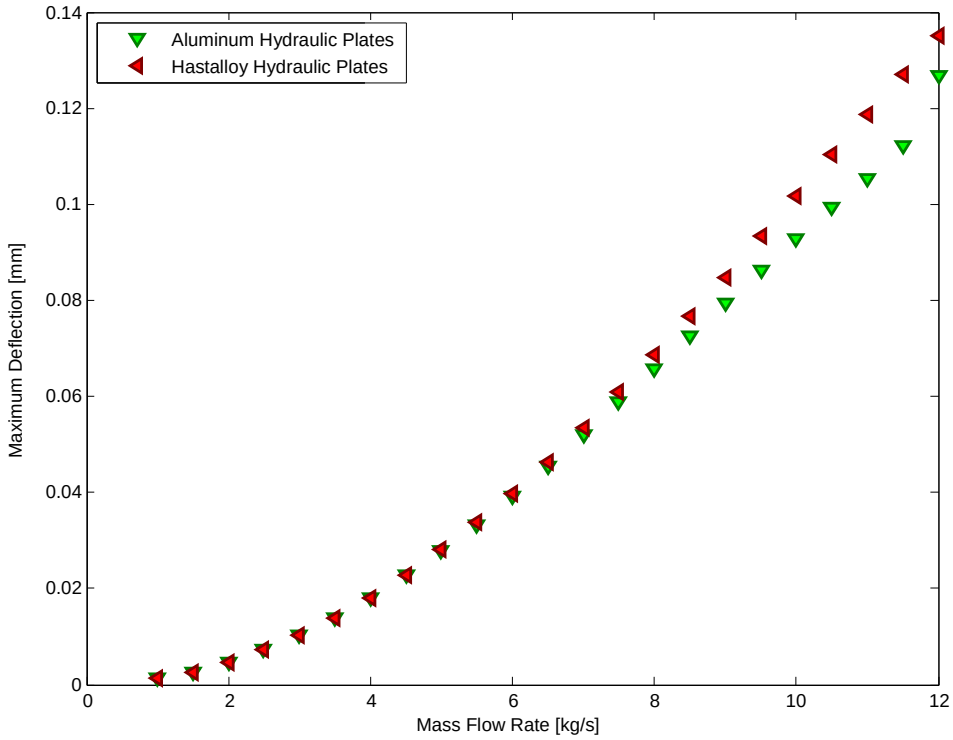

Figure 4.19: Comparison of test plate response with different hydraulic plates.

Figure 4.19 compares the maximum span-wise averaged deflection between an aluminum hydraulic plate condition and a Hastalloy plate condition. The rigid hydraulic plate condition sets up a limit for how much of an impact the Inconel plates could have. While

the change is relatively small at low flow rates, the results begin to diverge at higher flow rates, a consequence of the fixed boundaries being unable to deflect. While flow is diverted to other channels, the overall pressure difference causes the fuel plate to deflect more when the boundaries are fixed as opposed to deformable. What is interesting to note is the maximum deflection begins to converge again above Miller's critical velocity. The test plate deflects more under the rigid test plates because the hydraulic plates cannot deflect. Near and above Miller's velocity, the hydraulic plate deflections become a hindrance to the test plate deflection and result in an increased maximum deflection.

4.8 Heterogeneous Plate in the GTPA

While the parallel plate model provided works well for the aluminum model, it is of importance to compare the deflections witnessed in the homogeneous model to those of a heterogeneous model. The heterogeneous model plated model provided by Marcum et. al. [10] was used investigate the difference between a heterogeneous plate and a homogeneous plate. For the heterogeneous plate, the fuel material properties must be defined as well. These values are listed in Table 4.7 below.

Table 4.7: Additional parameters for the heterogeneous plate

Parameter (Symbol) [units]	Value
Plate thickness [a] (m)	0.00127
Young's modulus clad [E_c] (GPa)	70
Young's modulus fuel [E_f] (GPa)	87.27
Poisson's ratio clad [υ_c] (#)	0.33
Poisson's ratio fuel [υ_f] (#)	0.324
Clad thickness [a_1, a_3] (m)	0.0004445
Fuel thickness [a_2] (m)	0.000381
Spring constant [λ] (MN/m)	300

For all cases, the aluminum and fuel plate deflected less than 0.1% for every flow rate. The reason for the small change in the overall deflection is the slight difference between the flexural rigidity of the fuel plate and the aluminum plate. The fuel plate and the

aluminum plate in the center deflected less than in the entire array of aluminum. The stabilizing effect or the fuel plate can be seen in Figure 4.20.

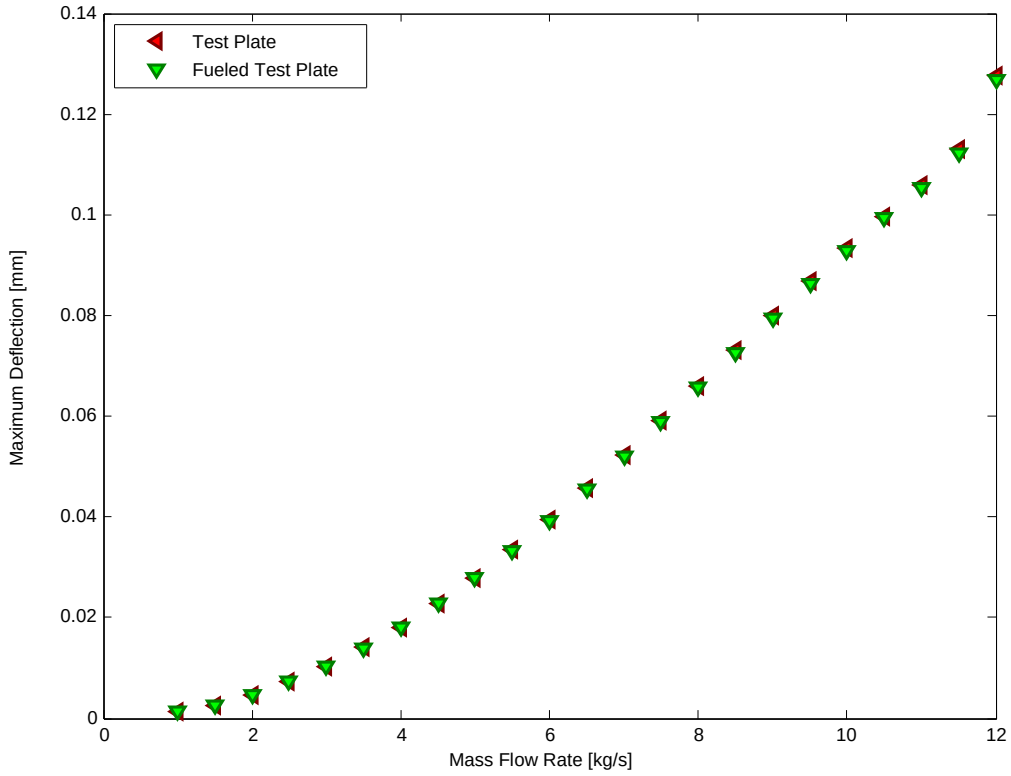

Figure 4.20: Comparison of homogeneous and heterogeneous models.

5 CONCLUSION

A new method for computing a plate's dynamic response to fluid in axial flow conditions has been detailed and presented herein. The method is compared against an analytic solution, a numerical model (ABAQUS), and experimental results. While the solutions yielded from the study do not produce a 'perfectly aligned' set of results as compared to the experimental and computational counterparts, the model does, in fact, produce representative solution forms which are founded on the transparency of the method.

Furthermore, the model provides a solution in the structural domain comparable to the solutions derived with ABAQUS. The largest discrepancy between the two models is at the entrance and exit of the plate. Despite the discrepancy, the deflection model still provides an accurate representation of the plate deflection. The greatest advantage of the study's model is its ability to achieve a solution within minutes utilizing much less processing power then an identical simulation using coupled CFD and FEM models which could take days.

The model also provides a solution for a parallel array of plates. The solution is achieved in a comparable amount of time as the single plate model, and given the resources required to run a large FSI simulation, the benefit is significant. The solution compares well with the post data for pressure drop, however, the change in gap height is very different. While the reason for this has been discussed, it is important to note that better data may provide better means of characterizing the overall deflections.

Additionally, use of the model has shown that the change in plate geometry from homogeneous to heterogeneous has played only a small roll on the overall deformation of the plate as the change in deflections between the aluminum and fuel plate were less than 0.1% at the highest achieved flow rate.

Lastly, a relation which credibly correlates appropriate minor losses at the inlet and exit of the flow channels would yield a more accurate solution, especially in the cases of as-built geometry where 'snap-through' and other leading-edge effects are prominent. The consequence of this can be seen in the case of the GTPA where the addition of a representative comb changed the plate profile significantly.

6 WORKS CITED

[1] J. C. Kennedy, C. J. Jesse and G. L. Solbrekken, "Experimental Investigation of Deflection of Flat Aluminium Plates Under Variable Velocity Parallel Flow," University of Missouri TherMec Research Group, Columbia, 2014.

[2] D. R. Miller, "Critical Flow Velocities for Collapse of Reactor Parallel-Plate Fuel Assemblies," Knolls Atomic Power Laboratory, Schenectady, 1958.

[3] W. L. Zabriskie, "An Experimental Evaluation of the Effect of Length-to-Width Ratio on the Critical Flow Velocity of Single Plate Assemblies," General Electric, Schenectady, 1959.

[4] G. Kim and D. C. Davis, "Hydrodynamic Instabilities in Flat-Plate-Type Fuel Assemblies," *Nuclear Engineering and Design*, vol. 158, pp. 1-17, 1995.

[5] P. Jensen and W. R. Marcum, "Predicting Critical Flow Velocity and Laminate Plate Collapse - Flat Plates," *Nuclear Engineering and Design*, vol. 267, pp. 71-87, 2014.

[6] C. Q. Guo and M. P. Paidoussis, "Stability of Rectangular Plates with Free Side-Edges in Two-Dimensional Inviscid Channel Flow," *Journal of Applied Mechanics*, vol. 67, pp. 171-176, Mar. 2000.

[7] C. Q. Guo and M. P. Paidoussis, "Analysis of Hydroelastic Instabilities of Rectangular Parallel-Plate Assemblies," *Journal of Pressure Vessel Technology,* vol. 122, pp. 502-508, Nov. 2000.

[8] W. Swinson and G. Yahr, "Dynamic Pressure Approach to Analysis of Reactor Fuel Plate Stability," Oak Ridge National Laboratory, Oak Ridge, 1990.

[9] R. D. Blevins, Flow-Induced Vibration, 2nd ed., New York: Van Nostrand Reinhold, 1990.

[10] C. Eloy, R. Lagrange, C. Souilliez and L. Schouveiler, "Aeroelastic Instability of Cantilevered Flexible Plates in Uniform Flow," *Journal of Fluid Mechanics,* vol. 611, pp. 97-106, 2008.

[11] S. Michelin and S. G. Llewellyn Smith, "Linear Stability Analysis of Coupled

Parallel Flexible Plates in an Axial Flow," *Journal of Fluids and Structures,* vol. 25, pp. 1136-1157, 2009.

[12] R. D. Groninger and J. J. Kane, "Flow Induced Deflectoins of Parallel Flat Plates," *Nuclear Science and Engineering,* pp. 218-226, 1963.

[13] W. L. Zabriskie, "An Experimental Evaluation of the Critical Flow Velocity Formulas for Parallel Plate Assemblies," General Engineering Laboratory, Schenectady, 1958.

[14] G. E. Smissaert, "Static and Dynamic Hydroelastic Instabilities in MTR-Type Fuel Experiments. Part I. Introduction and Experimental Investigation," *Nuclear Engineering and Design,* pp. 535-546, 1968.

[15] G. E. Smissaert, "Static and Dynamic Hydroelastic Instabilities in MTR-Type Fuel Elements Part II. Theoretical Investigatyion and Disccusion," *Nuclear Engineering and Design,* pp. 105-122, 1969.

[16] Z. D. Cui, Y. Q. Tang, C. Q. Guo, L. Yuan and C. L. Yan, "Flow-Induced Vibration and Stability of an Element Model for Parallel-Plate Fuel Assemblies," *Nuclear Engineering and Design,* vol. 238, pp. 1629-1635, 2008.

[17] W. Marcum, T. Holschuh and T. Howard, "On the Steady Mechanical Response of a Heterogeneous Fuel Plate," *Nuclear Technology,* 2015 [In Print].

[18] F. M. White, Fluid Mechanics, 7th ed., New York: McGraw Hill, 2011.

[19] O. C. Jones Jr., "An Improvement in the Calculation of Turbulent Friction in Rectangular Ducts," *Journal of Fluids Engineering,* pp. 173-181, 1976.

[20] J. J. Kane, "The Effect of Inlet Spacing Deviations on the Flow-Induced Deflections of Flat Plates," *Nuclear Science and Engineering,* pp. 305-308, 1962.

[21] R. Panton, Incompressible Flow, 3rd ed., Wiley, 2002.

[22] R. H. Nunn, Intermediate Fluid Mechanics, New York: Taylor & Francis Group, 1989.

[23] G. Roth, "CFD Analysis of Pressure Differentials in a Plate-type Fuel Assembly -

Thesis," Oregon State University, Corvallis, 2011.

[24] R. D. Blevins, Applied Fluid Dynamics Handbook, Malabar: Krieger Publishing Company, 2003.

[25] Special Metals Corporation, "INCONEL Alloy HX," Special Metals, Huntington, 2005.

7 NOMENCLATURE

7.1 Acronyms

ATR	Advanced Test Reactor
CFD	Computational Fluid Dynamics
CSM	Computational Structural Mechanics
FSI	Fluid-Structure Interaction
GTPA	Generic Test plate Assembly
GTRI	Global Threat Reduction Initiative
INL	Idaho National Lab

7.2 Variable

A	Cross sectional area (m^2)
a	Plate thickness (m)
b	Flow channel and plate width (m)
D	Flexural rigidity
Δ	Differential value
ε	Surface roughness (m)
E	Young's modulus (GPa)
F	Force, (N)
f	Friction Factor
∇	Gradient
h	Flow channel height (m)
I	Area moment of inertia
k	Form loss coefficient

l	Plate length (m)
λ	Spring constant (N/m)
$\dot{m}$	Mass flow rate [kg/s]
μ	Fluid viscosity (Pa-s)
υ	Poisson's ratio (#)
ϕ^*	Equation (28)
ρ	Fluid density (kg/m^3)
r	Equation (33)
Re	Reynolds number
v	Velocity (m/s)
v^*	Reduced Velocity
w	Plate Load (Pa)
x,y,z	Coordinate directions

7.3 Subscript

1	Flow channel 1
2	Flow channel 2
3	Inlet and outlet flow channel
c	Critical value
i	cell
n	Number of cells
r	Ratio value

8 APPENDIX A: MATLAB CODE

```
% Multiplate Flow Solver
% TKH 2/3/2015

%Here's some "ASCII" Pictures of the Plate Nomenclature
%/|                                                                          |\
%/|                                                                          |\
%/|XXXXXXXXXXXXXXXX|XXXXXXXXXXXXXXRegion 2cXXXXXXXXXXXXX|XXXXXXXXXXXXXXXX|\
%/|XXXXRegion 1XXXX|OOOOOOOOOOOOORegion 2bOOOOOOOOOOOOO|XXXXRegion 3XXXX|\
%/|XXXXXXXXXXXXXXXX|XXXXXXXXXXXXXXRegion 2aXXXXXXXXXXXXX|XXXXXXXXXXXXXXXX|\
%/|                                                                          |\
%/|                                                                          |\
%       z
%       |
%       |
%       |
%       /----------x
%      /
%     /
%    y
% Anticipated flow direction in y.



%////////////////////////////////////////////////////////////////////////
%________________________________________________________________________
%
% Gap 1
% FLOW
%------> XXXXXXXXXXXXXXXXXXXXXXXXPlateXXXXXXXXXXXXXXXXXXXXXXXX     Gap 3
%
% Gap 2
%________________________________________________________________________
%////////////////////////////////////////////////////////////////////////
%
%       z
%       |
%       |
%       |
%       /----------y
%      /
%     /
%    x

%1 Preliminary Values_____________________________________________________


%1.1 Initialization Parameters-------------------------------------------

clc %clears the screen
clear all %clears all variables
close all %closes the plots

% 1.2 User Input Variables-----------------------------------------------
```

```
% 1.2.1 Numerical and Discretizaition Parameters.....................
y_num = 64; %Number of cells in the Y direction, must be even
x_num = 65; %Number of cells in the X direction, should be odd
tolerance_f = 0.000000001; %friction factor tolerance (plate deflection loop)
tolerance_P = 1; %Pressure Tolerance (main loop)
tolerance_v = 0.000000001; %velocity tolerance (flow solver loop)

% 1.2.2 Geometric Variables..........................................

length = 0.6096; %[m] %length of the plate
width = 0.0889; %[m] %width of the plate
a = 0.00127; %[m] %Plate thickness
ref_h = 0.001905; %[m] %Reference Gap Size (should be close to average)
ref_A = ref_h*width; %[m^2] %Reference Gap Area
ref_P = 2*(width+ref_h); %[m] %Reference Gap Perimeter
ref_D = 4*ref_A/ref_P; %[m] %Reference Gap Diameter
%inlet_h = 0.022225; %[m] %Inlet Channel Height
%inlet_A = inlet_h*width; %[m^2] %Inlet Area
%inlet_P = 2*(inlet_h+width); %[m] %Inlet Perimeter
%inlet_D = 4*inlet_A/inlet_P; %[m] %Inlet Hydraulic Diameter
Channel_Data = csvread('channels_GTPA.csv'); %Channel Gap Probe Data
x_1 = 0.00635; %[m] %End of Region 1
x_2 = 0.09525; %[m] %End of Region 2(a,b,c)
x_3 = width; %End of Region 3, or the width of the plate


% 1.2.3 Flow/Fluid Properties........................................

P_o = 0; %Inlet Total_Pressure
rho = 990; %[kg/m^3] %fluid density
mu = 0.000553; %[Pa-s] %fluid dynamic viscosity
epsilon = 0.0000015; %[m/m] %pipe roughness
inlet_m = 6; %[kg/s] %inlet mass flow rate

% Plate Properties...................................................

%Set-up Parameters for Homogeneous Region 1
E = 70000000000; %[Pa] Young's Modulus
nu = 0.33; %[n/a] Poissons Ratio
G = E/(2*(1+nu)); %[Pa] Shear Modulus
flex = E*(a^3)/((12)*(1-(nu^2))); %Flexural Rigidity

% 1.3 Dependent Variables-------------------------------------------------

% 1.3.1 Calculated Parameters........................................
channel_num = numel(Channel_Data(1,:))-1; %[#] %Number of Channels
plate_num = channel_num-1; %[#] %Number of Plates

%Position Related Parameters
dy = length/y_num; %[m] %descritization length
dx = width/x_num; %[m] %descritization width
Y_Vector = (1:y_num)*dy-dy/2; %[m] %y vector of cell centers
Y_Vector_2(1:y_num+1) = ((1:y_num+1)-1)*dy; %[m] %y vector of cell edges
Y_Vector_3(1)=0; %[m] %y vector first point used for plotting pressure
Y_Vector_3(2:y_num+2) = ((1:y_num+1)-1)*dy; %[m] %ditto, for middle points
Y_Vector_3(y_num+3) = length; %[m] %ditto last point
X_Vector = ((1:x_num)*dx-dx/2)'; %[m] %x vector of cell centers
```

```
lambda = 300000000*0.0101203125^2/dy^2;

%Pre-allocation
Gap = zeros(y_num,channel_num);
Total_Pressure_Check = P_o*ones(y_num,channel_num);
Plate = zeros(y_num,plate_num);
Fluid_Load = Plate;
Plate_Load = Fluid_Load;
Self_Load = Plate_Load;
V_nom = ones(1,channel_num)*inlet_m/channel_num/rho/width/ref_h;
K_in = 0.5*ones(1,channel_num);
K_out = ones(1,channel_num);
F = 0.03*ones(y_num,channel_num);
Pi_f = ones(1,channel_num);
Profile = zeros(y_num,1);
Profile_Base = Profile;
for n = 1:channel_num
    Gap_Base(:,n) =
interp1(Channel_Data(:,1),Channel_Data(:,n+1),Y_Vector,'spline','extrap');
    Gap_Edge_Base(:,n) =
interp1(Channel_Data(:,1),Channel_Data(:,n+1),Y_Vector_2,'spline','extrap');
end
for n = 2:channel_num+1
    Profile_Base(:,n) = Gap_Base(:,n-1)+Profile_Base(:,n-1);
end
Gap_Edge = Gap_Edge_Base;
inlet_h = sum(Gap_Edge(1,:))+plate_num*a;
outlet_h = sum(Gap_Edge(y_num,:))+plate_num*a;
alpha = 0.1;
for inlet_m = 12

    residual_P = 100;
    while residual_P > tolerance_P
        Deflection = Plate_Load/(720*flex)*width^4;
        for n = 2:y_num-1
            Delta_z(n,:) = Deflection(n-1,:)-
2*Deflection(n,:)+Deflection(n+1,:);
        end
        Delta_z(1,:) = 0-5*Deflection(1,:)+Deflection(2,:);
        Delta_z(y_num,:) = Deflection(y_num-1,:)-5*Deflection(y_num,:)+0;
        Self_Load = lambda*Delta_z;
        Gap(:,1) = Gap_Base(:,1)+Deflection(:,1);
        Gap(:,channel_num) = Gap_Base(:,channel_num)-Deflection(:,plate_num);
        if plate_num > 1
            for n = 2:plate_num
                Gap(:,n) = Gap_Base(:,n)+Deflection(:,n)-Deflection(:,n-1);
                Gap_Edge(:,n) =
interp1(Y_Vector,Gap(:,n),Y_Vector_2,'spline','extrap');
            end
        end
        Ratio_v = ref_h./Gap;
        Ratio_h = Gap/ref_h;
        for n = 1:channel_num
            Gap_Edge(:,n) =
interp1(Y_Vector,Gap(:,n),Y_Vector_2,'spline','extrap');
            Ratio_v_in(1,n) = ref_h./Gap_Edge(1,n);
            Ratio_v_out(1,n) = ref_h./Gap_Edge(1+y_num,n);
            Ratio_h_in(1,n) = Ratio_v_in(1,n)^-1;
            Ratio_h_out(1,n) = Ratio_v_out(1,n)^-1;
```

```
        end
        D = 4*width*Gap./(2*(width+Gap));
        residual_v = 1;
        while residual_v > tolerance_v
            for n = 1:channel_num
                Re = rho*V_nom(n)*Ratio_v.*D/mu;
            end
            phi_star = 2/3+11/24*Gap/width.*(2-Gap/width);
            Re_star = phi_star.*Re;
            F = (-2.0*log10(epsilon./D/3.7+2.51./(Re_star.*F.^(1/2)))).^-2;
            for n = 1:channel_num
                Inlet_h_eff(n) = inlet_h*rho*width*ref_h*V_nom(n)/inlet_m;
                Outlet_h_eff(n) = outlet_h*rho*width*ref_h*V_nom(n)/inlet_m;
                K_in(n) = 0.6+0*(1-Ratio_h_in(n)*ref_h/Inlet_h_eff(n))^2;
                K_out(n) = 1.6+0*(1-Ratio_h_out(n)*ref_h/Outlet_h_eff(n))^2;
            end
            Pi_f =
(sum(((Ratio_v.^2).*F*dy)./D)+K_in.*(Ratio_v_in.^2)+K_out.*(Ratio_v_out.^2));
            pressure_drop = 1/2*rho*V_nom(1)^2*Pi_f(1);
            for n = 1:channel_num
                V_nom(n) = (2*pressure_drop/rho/Pi_f(n))^(1/2);
            end
            outlet_m = rho*sum(V_nom)*ref_h*width;
            V_nom(1) = V_nom(1)*inlet_m/outlet_m;
            parameter_3 = 0;
            while parameter_3 > tolerance_f
            end
            residual_v = abs(inlet_m-outlet_m)/inlet_m;
        end
        for n = 1:channel_num
            Total_Pressure_Check(2,n) = Total_Pressure_Check(1,n)-
1/2*rho*(Ratio_v_in(n)*V_nom(n))^2*K_in(n);
            for m = 3:y_num+2
                Total_Pressure_Check(m,n) = Total_Pressure_Check(m-1,n)-
1/2*rho*(Ratio_v(m-2,n)*V_nom(n))^2*(F(m-2,n)*dy/D(m-2,n));
            end
            Total_Pressure_Check(y_num+3,n) = Total_Pressure_Check(y_num+2,n)-
1/2*rho*(Ratio_v_out(n)*V_nom(n))^2*K_out(n);
        end
        for n = 1:channel_num
            Total_Pressure(:,n) =
interp1(Y_Vector_3(2:y_num+2),Total_Pressure_Check(2:y_num+2,n),Y_Vector,'linea
r');
            Dynamic_Pressure(:,n) = 1/2*rho*(Ratio_v(:,n)*V_nom(n)).^2;
            Static_Pressure(:,n) = Total_Pressure(:,n)-Dynamic_Pressure(:,n);
        end
        for n = 1:plate_num
            Fluid_Load(:,n) = Static_Pressure(:,n)-Static_Pressure(:,n+1);
        end

        Plate_Load = alpha*(Fluid_Load+Self_Load)+(1-alpha)*Plate_Load;
        residual_P = max(max(abs((Plate_Load-(Self_Load+Fluid_Load)))))/alpha;
        for n = 2:channel_num+1
            Profile(:,n) = Gap(:,n-1)+Profile(:,n-1);
        end

    end

end
```